HAL open science

Tracing Lyα and LyC Escape in Galaxies with Mg II Emission

Xinfeng Xu, Alaina Henry, Timothy Heckman, John Chisholm, Gábor Worseck, Max Gronke, Anne Jaskot, Stephan R. Mccandliss, Sophia R. Flury, Mauro Giavalisco, et al.

To cite this version:

Xinfeng Xu, Alaina Henry, Timothy Heckman, John Chisholm, Gábor Worseck, et al.. Tracing Lyα and LyC Escape in Galaxies with Mg II Emission. The Astrophysical Journal, 2022, 933, 10.3847/1538-4357/ac7225 . insu-03777339

HAL Id: insu-03777339

https://insu.hal.science/insu-03777339

Submitted on 15 Sep 2022

HAL is a multi-disciplinary open access archive for the deposit and dissemination of scientific research documents, whether they are published or not. The documents may come from teaching and research institutions in France or abroad, or from public or private research centers.

L'archive ouverte pluridisciplinaire **HAL**, est destinée au dépôt et à la diffusion de documents scientifiques de niveau recherche, publiés ou non, émanant des établissements d'enseignement et de recherche français ou étrangers, des laboratoires publics ou privés.

Distributed under a Creative Commons Attribution 4.0 International License

The Astrophysical Journal, 933:202 (22pp), 2022 July 10 https://doi.org/10.3847/1538-4357/ac7225
© 2022. The Author(s). Published by the American Astronomical Society.
OPEN ACCESS

Tracing Lyα and LyC Escape in Galaxies with Mg II Emission

Xinfeng Xu[1], Alaina Henry[1,2], Timothy Heckman[1], John Chisholm[3], Gábor Worseck[4], Max Gronke[5], Anne Jaskot[6], Stephan R. McCandliss[1], Sophia R. Flury[7], Mauro Giavalisco[8], Zhiyuan Ji[8], Ricardo O. Amorín[9], Danielle A. Berg[3], Sanchayeeta Borthakur[10], Nicolas Bouche[11], Cody Carr[12], Dawn K. Erb[13], Harry Ferguson[2], Thibault Garel[14], Matthew Hayes[15], Kirill Makan[4], Rui Marques-Chaves[14], Michael Rutkowski[16], Göran Östlin[15], Marc Rafelski[1,2], Alberto Saldana-Lopez[14], Claudia Scarlata[12], Daniel Schaerer[14], Maxime Trebitsch[17], Christy Tremonti[18], Anne Verhamme[14], and Bingjie Wang[1]

[1] Center for Astrophysical Sciences, Department of Physics & Astronomy, Johns Hopkins University, Baltimore, MD 21218, USA; xinfeng@jhu.edu
[2] Space Telescope Science Institute, 3700 San Martin Drive, Baltimore, MD 21218, USA
[3] Department of Astronomy, The University of Texas at Austin, 2515 Speedway, Stop C1400, Austin, TX 78712, USA
[4] Institut für Physik und Astronomie, Universität Potsdam, Karl-Liebknecht-Str. 24/25, D-14476 Potsdam, Germany
[5] Max-Planck Institute for Astrophysics, Karl-Schwarzschild-Str. 1, D-85741 Garching, Germany
[6] Department of Astronomy, Williams College, Williamstown, MA 01267, USA
[7] Department of Astronomy, University of Massachusetts Amherst, Amherst, MA 01002, USA
[8] Department of Astronomy, University of Massachusetts Amherst, 710 N. Pleasant Street, Amherst, MA 01003, USA
[9] Instituto de Investigacion Multidisciplinar en Ciencia y Tecnologia, Universidad de La Serena, Raul Bitran 1305, La Serena, Chile
[10] School of Earth & Space Exploration, Arizona State University, Tempe, AZ 85287, USA
[11] Univ Lyon, Univ Lyon1, ENS de Lyon, CNRS, Centre de Recherche Astrophysique de Lyon (CRAL) UMR5574, 69230, Saint-Genis-Laval, France
[12] Minnesota Institute for Astrophysics, School of Physics and Astronomy, University of Minnesota, 316 Church Street SE, Minneapolis, MN 55455, USA
[13] Center for Gravitation, Cosmology and Astrophysics, Department of Physics, University of Wisconsin Milwaukee, 3135 N. Maryland Avenue, Milwaukee, WI 53211, USA
[14] Department of Astronomy, University of Geneva, 51 Chemin Pegasi, 1290 Versoix, Switzerland
[15] Department of Astronomy, Oskar Klein Centre, Stockholm University, SE-106 91 Stockholm, Sweden
[16] Department of Physics and Astronomy, Minnesota State University, Mankato, MN 56001, USA
[17] Kapteyn Astronomical Institute, University of Groningen, P.O. Box 800, 9700 AV Groningen, The Netherlands
[18] Department of Astronomy, University of Wisconsin–Madison, Madison, WI 53706, USA
Received 2022 February 16; revised 2022 May 18; accepted 2022 May 19; published 2022 July 14

Abstract

Star-forming galaxies are considered the likeliest source of the H I ionizing Lyman continuum (LyC) photons that reionized the intergalactic medium at high redshifts. However, above $z \gtrsim 6$, the neutral intergalactic medium prevents direct observations of LyC. Therefore, recent years have seen the development of *indirect* indicators for LyC that can be calibrated at lower redshifts and applied in the epoch of reionization. Emission from the Mg II $\lambda\lambda$2796, 2803 doublet has been proposed as a promising LyC proxy. In this paper, we present new Hubble Space Telescope/Cosmic Origins Spectrograph observations for eight LyC emitter candidates, selected to have strong Mg II emission lines. We securely detect LyC emission in 50% (4/8) of the galaxies with 2σ significance. This high detection rate suggests that strong Mg II emitters might be more likely to leak LyC than similar galaxies without strong Mg II. Using photoionization models, we constrain the escape fraction of Mg II as ~15%–60%. We confirm that the escape fraction of Mg II correlates tightly with that of Lyα, which we interpret as an indication that the escape fraction of both species is controlled by resonant scattering in the same low column density gas. Furthermore, we show that the combination of the Mg II emission and dust attenuation can be used to estimate the escape fraction of LyC statistically. These findings confirm that Mg II emission can be adopted to estimate the escape fraction of Lyα and LyC in local star-forming galaxies and may serve as a useful indirect indicator at the epoch of reionization.

Unified Astronomy Thesaurus concepts: Ultraviolet astronomy (1736); Starburst galaxies (1570); Interstellar dust (836); Reionization (1383); Emission line galaxies (459)

1. Introduction

The epoch of reionization (EOR) was one of the last major phase transitions of the universe, marked by the emergence of the first galaxies and the ionization of the neutral hydrogen (H I) in the intergalactic medium (IGM). Though it has been widely recognized from various observations that the EOR happened at $z \sim 6$–9 (e.g., Becker et al. 2001; Fan et al. 2006; Bañados et al. 2018; Mason et al. 2018; Planck Collaboration et al. 2020), the types of sources that were responsible for the majority of ionizing photons remain elusive.

High-luminosity active galactic nuclei (AGNs) or quasars are appealing sources of ionizing photons. However, the number of quasars at high z is too low to reionize the whole universe (e.g., Hopkins et al. 2008; Madau & Haardt 2015; Matsuoka et al. 2018; Kulkarni et al. 2019; Shen et al. 2020; Trebitsch et al. 2021). Although the contribution from unobserved low-luminosity AGNs is still debated (Giallongo et al. 2015; Matsuoka et al. 2018; Parsa et al. 2018; Grazian et al. 2020), star-forming (SF) galaxies are usually considered the likeliest candidates since they substantially outnumber quasars (e.g., Madau & Dickinson 2014; Shen et al. 2020). Critically, however, it has not yet been demonstrated that SF galaxies can

Original content from this work may be used under the terms of the Creative Commons Attribution 4.0 licence. Any further distribution of this work must maintain attribution to the author(s) and the title of the work, journal citation and DOI.

contribute enough H I ionizing Lyman continuum (LyC) photons to ionize the IGM. Moreover, it is still unclear whether the reionization was dominated by brighter, more massive galaxies or the more numerous population of faint SF galaxies (e.g., Finkelstein et al. 2019; Naidu et al. 2020).

The ionizing photon budget is commonly described as the product of three parameters: the UV luminosity density of either AGNs or SF galaxies ($\rho_{\rm UV}$, erg s^{-1} Hz^{-1} Mpc^{-3}), the ionizing photon production efficiency ($\xi_{\rm ion}$, photons erg^{-1} Hz), and the fraction of ionizing photons that escape from galaxies ($f_{\rm esc}^{\rm LyC}$, %; see, e.g., Madau et al. 1999; Robertson et al. 2013; Duncan & Conselice 2015). Parameters $\xi_{\rm ion}$ and $\rho_{\rm UV}$ have been or can be mostly constrained (e.g., Chevallard et al. 2018; Berg et al. 2019; Tang et al. 2019; Bouwens et al. 2021). Models using current estimations of $\xi_{\rm ion}$ and $\rho_{\rm UV}$ suggest that $f_{\rm esc}^{\rm LyC}$ needs to be >5%–20% on average for SF galaxies to reionize the universe (e.g., Robertson et al. 2013, 2015; Rosdahl et al. 2018; Finkelstein et al. 2019; Naidu et al. 2020). However, inferring $f_{\rm esc}^{\rm LyC}$ for high-z galaxies is extremely challenging owing to the absorption of the LyC photons by (1) its short mean free path to the high incidence of Lyman limit systems for $4 \lesssim z \lesssim 6$ (e.g., Worseck et al. 2014; Becker et al. 2021) and (2) the neutral IGM for $z \gtrsim 6$ (e.g., Inoue et al. 2014). Thus, observations at lower redshifts must develop indirect indicators for $f_{\rm esc}^{\rm LyC}$, which can then be applied to EOR galaxies.

During the past decade, considerable efforts have been made toward measuring $f_{\rm esc}^{\rm LyC}$ at low redshifts, mainly adopting observations from the Far Ultraviolet Spectroscopic Explorer (FUSE; e.g., Heckman et al. 2001; Bergvall et al. 2006; Leitet et al. 2013; Borthakur et al. 2014) and Hubble Space Telescope/Cosmic Origins Spectrograph (HST/COS; e.g., Izotov et al. 2016a, 2016b; Leitherer et al. 2016; Puschnig et al. 2017; Izotov et al. 2018a, 2018b; Wang et al. 2019; Izotov et al. 2021; Flury et al. 2022a, 2022b). Various indirect indicators of $f_{\rm esc}^{\rm LyC}$ have also been proposed (see a summary in Flury et al. 2022b). For example, the [O III] λ5007/[O II] λ3727 flux ratio (O32) may be an indicator of the ionization state of the interstellar medium (ISM), with high O32 values suggesting low optical depth in neutral gas (e.g., Jaskot & Oey 2013; Oey et al. 2015; Nakajima et al. 2020). Alternatively, star formation rate (SFR) surface density ($\Sigma_{\rm SFR}$) is postulated to relate to galaxy outflows, which can clear holes in the ISM to allow LyC escape (e.g., Heckman et al. 2011; Borthakur et al. 2014; Alexandroff et al. 2015; Trebitsch et al. 2017; Saldana-Lopez et al. 2022).

One of the leading indirect indicators is Lyα emission (e.g., Henry et al. 2015; Verhamme et al. 2015; Dijkstra et al. 2016; Verhamme et al. 2017; Jaskot et al. 2019; Gazagnes et al. 2020; Kakiichi & Gronke 2021). Lyα photons resonantly scatter so that their emergence from galaxies is strongly influenced by the reservoir of neutral hydrogen in/around the galaxy. The scattering alters the intrinsic Lyα emission line profile and, at the same time, imprints valuable information about H I onto the modified line profile. In particular, the presence of double-peaked Lyα profiles and the separation between the blue and red peaks have been demonstrated to correlate with $f_{\rm esc}^{\rm LyC}$ (e.g., Izotov et al. 2018b; Gazagnes et al. 2020). However, for high-z galaxies ($z \gtrsim 4$), the neutral IGM can absorb a large amount of the Lyα photons, in particular their blue peaks (usually the weaker peak). Therefore, the interpretation of Lyα profiles at high z can be challenging (e.g., Stark et al. 2011; Schenker et al. 2014; Gronke et al. 2021; Hayes et al. 2021).

In this paper, we further study Mg II as an indirect indicator for tracing the escape of Lyα and LyC. This idea has been proposed in Henry et al. (2018) and also studied in Chisholm et al. (2020). Mg II has a doublet transition at 2796.35 and 2803.53 Å and is similar to Lyα as an indirect indicator because (1) Mg II is a low-ionization transition and has an ionization potential (to destroy Mg II) of 15.03 eV, which is close to that of destroying H I ($\simeq$13.6 eV), and (2) Mg II is also a resonant line, whose line profile could contain information about the neutral gas of the galaxy. Therefore, Mg II can be used to trace the neutral hydrogen in/around the galaxy. Furthermore, compared to Lyα, Mg II has three advantages: (1) given that the IGM is mostly unpolluted by metals in the EOR (Rafelski et al. 2014), Mg II is much less attenuated by the neutral IGM than Lyα; (2) the doublet line ratio of Mg II λ2796/Mg II λ2803 is related to the Mg II optical depth (Chisholm et al. 2020) and is insensitive to the dust extinction given the close wavelengths of the two lines; and (3) at high z, the Mg II $\lambda\lambda$2796, 2803 doublet is redshifted to wavelengths observable by the James Webb Space Telescope (JWST). These advantages, combined with the moderate brightness of Mg II (~10%–60% of Hβ; Guseva et al. 2013), could allow us to detect Mg II emission in the distant universe.

The structure of the paper is as follows. In Section 2, we introduce the sample selection of Mg II, as well as the observations and data reductions. We also show various basic measurements from the spectra in Section 2. In Section 3, we discuss the two main geometries that allow Mg II, Lyα, and LyC photons to escape and then present how to measure their escape fractions separately. In Section 4, we present possible correlations between Mg II and Lyα and LyC, and we also discuss how we can predict $f_{\rm esc}^{\rm LyC}$ from the observed Mg II emission lines. We then discuss the high detection rates of LyC in our sample and [S II] deficiency in Section 5. In Section 6, we conclude the paper and discuss possible future work.

2. Observations, Data Reduction, and Basic Measurements

2.1. Sample Selection

To study Mg II along with the observed Lyα and LyC features, we need to detect three different spectral regions for each galaxy. Therefore, we have selected our sample of Mg II emitters from Sloan Digital Sky Survey (SDSS-IV)/eBOSS and obtained follow-up observations of their Lyα and LyC spectral regions with HST/COS. The main selection criteria are as follows: (1) we require GALEX near-UV (NUV) detections, with NUV < 22 AB; (2) we choose galaxies with Hβ equivalent width (EW) >5 Å to remove passive galaxies; (3) the redshifts of the galaxies were chosen to be in the range of $0.32 < z < 0.45$, which allows us to detect the Mg II $\lambda\lambda$2796, 2803 doublet from the SDSS/eBOSS spectra, the Lyα lines from the COS/G160M spectra, and LyC features from the COS/G140L spectra; (4) then, we require Mg II emission at $\gtrsim 7\sigma$ significance, in order to ensure that we are not proposing follow-up of spurious detections; (5) we require Mg II EW $\gtrsim$ 10 Å (for the summed doublet lines), which returns the most extreme Mg II emitters, reaching relatively unexplored parameter space; and (6) galaxies with AGN activity were excluded using the line ratios and the BPT diagrams (Baldwin et al. 1981). These criteria lead to a parent sample of 22 objects from eBOSS. Then, we select eight objects with NUV magnitudes brighter than 21.6, which can be

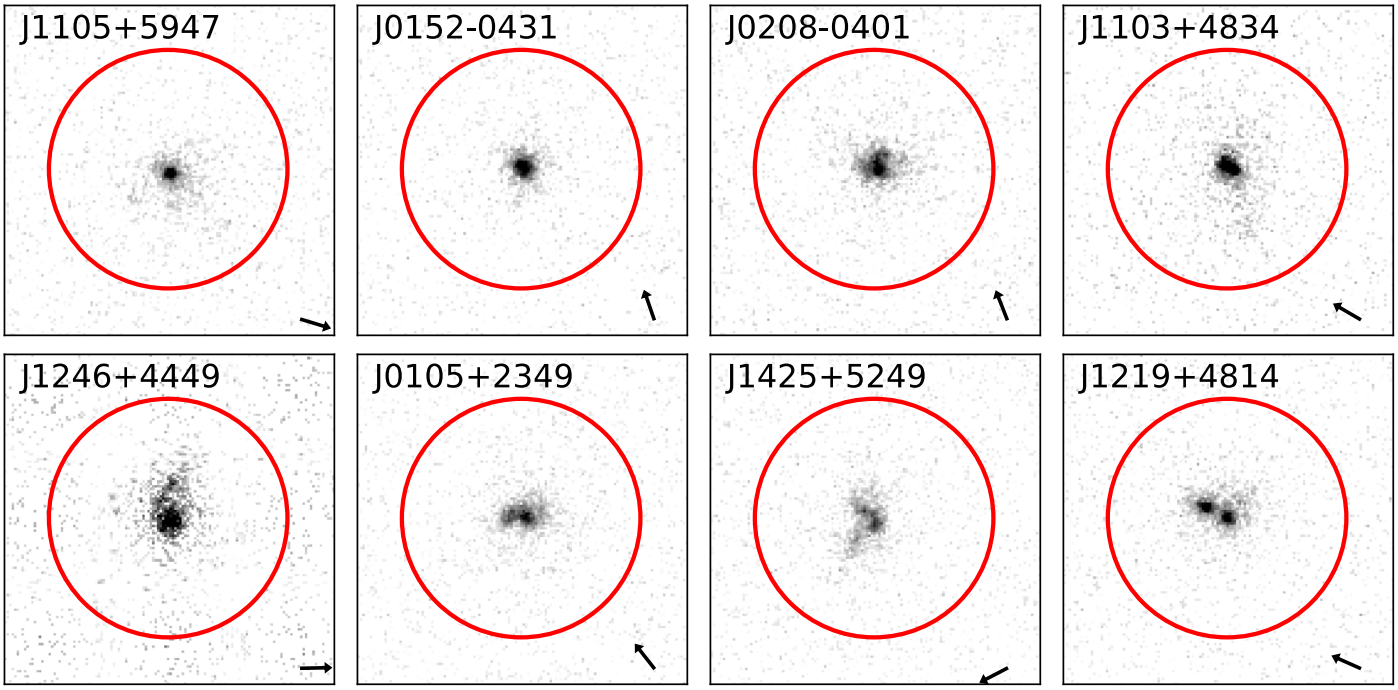

Figure 1. The HST/COS NUV acquisition images for galaxies in our sample. For each panel, we overlay the COS aperture with a diameter of 2.″5 as the red circle and denote the spectral dispersion axis by the black arrow. Objects are ordered by the measured escape fraction of Lyman continuum ($f_{\rm esc}^{\rm LyC}$; see Section 3.1.1), while the last two objects have $f_{\rm esc}^{\rm LyC}$ as upper limits.

Table 1
HST Observations and Basic Properties for Galaxies in Our Sample

ID	R.A.	Decl.	z[a]	G140L[b] (s)	G160M[b] (s)	SDSS-u[c] (mag)	NUV[d] (mag)	FUV[d] (mag)	$E(B-V)_{\rm MW}$[e]
J0105+2349	01:05:33.74	+23:49:59.63	0.3381	4500	2500	21.45	21.52	21.82	0.034
J0152–0431	01:52:07.99	–04:31:17.17	0.3836	1700	2500	21.65	21.30	21.50	0.036
J0208–0401	02:08:18.90	–04:01:36.37	0.3844	7200	2500	21.50	21.29	21.35	0.021
J1103+4834	11:03:59.00	+48:34:55.95	0.4180	2000	2600	21.21	21.19	21.66	0.014
J1105+5947	11:05:06.33	+59:47:41.37	0.4054	2000	2700	21.59	21.30	22.05	0.007
J1219+4814	12:19:47.85	+48:14:10.59	0.4203	1900	2600	21.26	21.23	21.48	0.011
J1246+4449[f]	12:46:19.49	+44:49:02.43	0.3222	1600	2000	20.28	20.17	20.55	0.021
J1425+5249	14:25:35.11	+52:49:02.18	0.3870	2600	4900	21.90	21.58	21.92	0.007

Notes.
[a] Redshift of the objects derived from Gaussian fits to the Balmer emission lines.
[b] Exposure time in seconds for HST COS/G140L and G160M gratings (HST-GO: 15865; PI: Henry).
[c] The u-band magnitudes from SDSS photometry.
[d] NUV and far-UV (FUV) band magnitude from GALEX photometry, respectively.
[e] MW dust extinction obtained from the Galactic Dust Reddening and Extinction Map (Schlafly & Finkbeiner 2011) at NASA/IPAC Infrared Science Archive.
[f] The COS/G140L observation of J1246+4449 is from the archival data (LzLCS survey, GO: 15626; PI: Jaskot).

observed in a relatively short time by HST (one to four orbits). The final selected objects are listed in Table 1.

2.2. COS Observations and Reduction

The eight galaxies in our sample were observed during HST Cycle 27 through project HST-GO-15865 (PI: Henry). This program obtained COS G140L and G160M observations that probed the LyC and Lyα regions, respectively. One of the eight galaxies (J1246+4449) overlaps with the Low-redshift Lyman Continuum Survey (LzLCS, HST GO: 15626; PI: Jaskot; Flury et al. 2022a), so we use the archival LyC observations for this object (but we still acquired new G160M observations). The details of observations are listed in Table 1.

In Figure 1, we show the HST/COS acquisition images for galaxies in our sample. We overlay the COS aperture size (2.″5 in diameter) as the red circles. The compact NUV light profiles of our galaxies are contained within the COS aperture. These compact features are similar to the Green Pea (GP) galaxies (e.g., Henry et al. 2015, 2018; Jaskot et al. 2019). We present several basic galaxy properties in Table 2.

To get robust estimates of the LyC flux from the HST/COS G140L spectra, we follow the reduction methods in previous publications (Wang et al. 2019; Flury et al. 2022a). We use the standard CALCOS pipeline (v3.3.9) and further estimate the dark current and scattered geocoronal Lyα background adopting the custom software FaintCOS (Makan et al. 2021). For HST/COS G160M data, we directly download the reduced

Table 2
Derived Properties for Galaxies in Our Sample

ID	CFWHM[a] (arcsec)	r_{50}[b] (kpc)	SFR[c] ($M_\odot$ yr^{-1})	$\Sigma_{\rm SFR}$[d] ($M_\odot$ yr^{-1} kpc^{-2})	$M_{\rm UV}$[e] (mag)
J0105+2349	1.08	0.85	16.6	1.8	−19.94
J0152–0431	0.18	0.66	13.6	2.5	−20.27
J0208–0401	0.54	0.79	13.2	1.7	−20.32
J1103+4834	0.72	0.70	24.3	4.0	−20.64
J1105+5947	0.36	0.68	6.9	1.2	−20.24
J1219+4814	0.90	1.25	18.0	0.9	−20.37
J1246+4449	1.44	0.82	25.2	3.0	−20.85
J1425+5249	0.72	1.19	9.2	0.5	−19.83

Notes.
[a] FWHM measured in the cross-dispersion direction around the galaxy's Lyα emission lines.
[b] Half-light radius of the galaxy measured from the HST/COS NUV acquisition images (see Figure 1).
[c] SFR of the galaxy derived from Hβ emission lines (Kennicutt & Evans 2012).
[d] SFR surface density.
[e] Absolute AB magnitude measured around 1500 Å rest frame and corrected for MW extinction.

data from the HST/MAST archive. For each galaxy, we have also checked the 2D G160M spectra and find that Lyα is completely covered in the COS extraction aperture.

We then correct both G140L and G160M spectra for Milky Way (MW) extinction using the Galactic Dust Reddening and Extinction Map (Schlafly & Finkbeiner 2011) at the NASA/IPAC Infrared Science Archive assuming the extinction law from Cardelli et al. (1989). The final reduced spectral regions of LyC (from G140L data) are shown in Figure 2, while the Lyα regions (from G160M data) are shown in Figure 3.

2.3. Basic Measurements from COS and SDSS Spectra

In the following subsections, we discuss how we conduct basic measurements of the HST/COS and SDSS data.

2.3.1. The Observed LyC Flux

In the literature, flux in the Lyman continuum (F(LyC)) is usually measured as the average flux over a window ($\sim$20 Å in the rest frame) close to and shortward of the Lyman limit (e.g., Izotov et al. 2021; Flury et al. 2022a, 2022b). Due to the redshift range of our galaxies, a few of the LyC regions are close to geocoronal Lyα emission lines. To minimize the contamination from geocoronal Lyα, we measure F(LyC) from two windows that are both away from the geocoronal lines. The blue window is set to be 20 Å wide in the rest frame and $<$ 1180 Å in the observed frame. The red window is between 1250 Å and the Lyman limit (912 Å $\times$ (1 + z)) in the observed frame. These two sets of windows are shown as the blue and red horizontal lines in Figure 2. Then, we measure the average flux within the blue and red windows and report them as $F(\mathrm{LyC})_B$ and $F(\mathrm{LyC})_R$, respectively, in Table 3. The 1σ error bars are computed by sampling from the Poisson distributions of the background and science spectra following the methodology in Feldman & Cousins (1998). For galaxies with the Lyman limit close to 1250 Å, the widths of the red windows are narrower (in J0152–0431, J0208–0401, and J1425+5249). For galaxies that have Lyman limits $<$ 1250 Å, no $F(\mathrm{LyC})_R$ is reported (J0105+2349 and J1246+4449) owing to the heavy contamination from geocoronal Lyα.

In Table 3, among the six galaxies that have F(LyC) measured in both windows, five have $F(\mathrm{LyC})_B$ and $F(\mathrm{LyC})_R$ that are all consistent within 2σ (all except J0152–0431). Given this general consistency of measured LyC flux from two windows, we adopt the $F(\mathrm{LyC})_R$ when there exists a red window. This is also the common choice in literature, i.e., measuring LyC flux as close as possible to the Lyman limit. For the two galaxies (J0105+2349 and J1246+4449) that do not have $F(\mathrm{LyC})_R$, we adopt their measured $F(\mathrm{LyC})_B$. These adopted F(LyC) values are shown in boldface in Table 3.

We take the same criteria to define an LyC detection as in LzLCS (Flury et al. 2022a), i.e., galaxies with LyC flux detected at the $>$2σ level. In this case, four out of our eight galaxies are classified as detections. For J0152–0431, its $F(\mathrm{LyC})_R$ and $F(\mathrm{LyC})_B$ are only consistent within 3σ, and $F(\mathrm{LyC})_B$ is consistent with 0 (which could be due to the absorption of Lyman series from an IGM cloud at $z \sim 0.26$). Therefore, we treat it along with J1246+4449 (which has $\sim$1.8σ on F(LyC)) as the two tentative cases. For the other two objects (J1219+4814 and J1425+5249), F(LyC) is consistent with zero, so we report their 2σ upper limits in Table 3. Overall, for our sample, the LyC detection rate ($>$2σ) is at least $4/8 = 50\%$.

2.4. Measurements of the Lyα Features

We measure the continuum flux[19] for the Lyα spectral region by adopting a linear fit to the continuum $\sim \pm 2000$ km s^{-1} around the systemic velocity. Then, we measure the flux, EWs, and peak velocities from the Lyα profiles. For each measured parameter, the corresponding errors are estimated through a Monte Carlo (MC) simulation where we perturb the spectrum 10^4 times according to the observed 1σ uncertainties. These measurements are reported in Table 4. The Lyα profiles for our galaxies are shown in Figure 3.

We have also tested possible contaminations from stellar features (e.g., stellar Lyα absorption) by subtracting the Lyα spectral regions by our best-fitted SED models discussed in Section 3.1.1 and remeasuring the line parameters for Lyα. We find that EW(Lyα) only has small changes, while flux and peak velocities stay almost unchanged. This is because our Lyα emission lines are strong compared to the stellar absorption. Therefore, we conclude that the contaminations from stellar absorption are minimal, and we do not correct Lyα by stellar

[19] In HST/COS G160M spectra for our galaxies, the continuum flux for Lyα regions usually approaches 0.

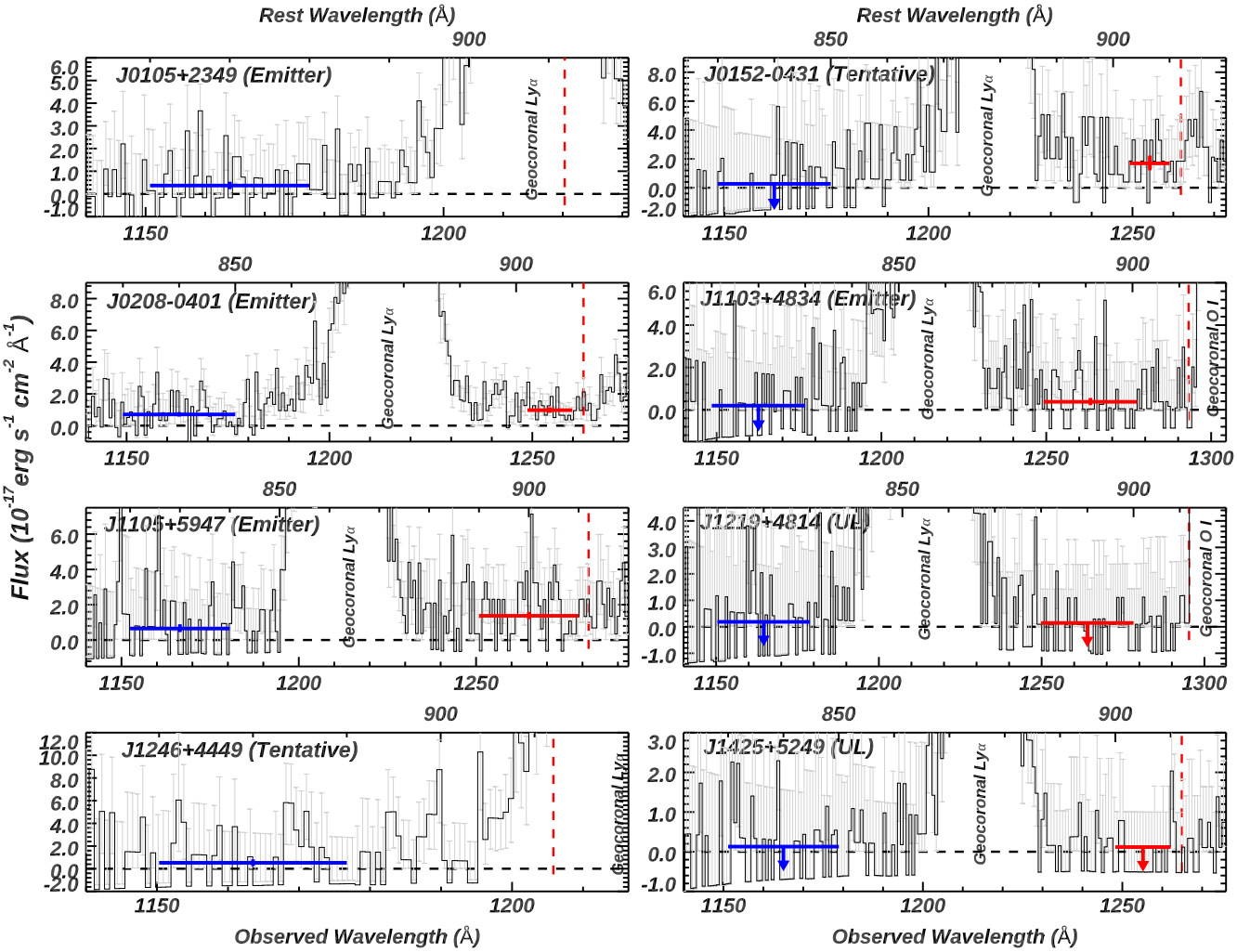

Figure 2. The reduced spectra for the LyC regions (corrected for MW extinction). The HST/COS spectra are in black, while their errors are shown in gray. The location of the Lyman limit is indicated by the vertical red dashed lines. Strong geocoronal lines (Lyα and O I λ1302) are labeled. To minimize the contamination from geocoronal Lyα, we measure the flux of LyC from the blue and red windows that are away from the geocoronal Lyα. For each galaxy, the mean LyC flux is calculated by averaging the flux within a window that is shown with the horizontal blue or red lines. The corresponding uncertainties are indicated by the vertical solid line, or as arrows if no detections. Based on the measured LyC flux, we classify and label galaxies into three categories, i.e., LyC emitters, tentative LyC emitters, and upper limits (UL) on LyC. See details in Section 2.3.1.

features. This is also consistent with previous studies that we will compare in Section 4.

For all objects in our sample, we detect double-peaked features in Lyα. The velocity separation of the peaks has been found to correlate with LyC photon escape (e.g., Verhamme et al. 2015; Gronke et al. 2016; Orlitová et al. 2018; Jaskot et al. 2019; Gazagnes et al. 2020, and see Section 4.4). We measure the velocities of both peaks compared to the systemic velocity and also report them in Table 4. Note that some of the galaxies' Lyα profiles may exhibit more than two peaks, and we return to this feature in Section 4.4.

2.5. Measurements of the SDSS Spectra

We retrieved the SDSS spectra for each of the galaxies in our sample and conducted a variety of measurements from the optical emission lines as follows. The Mg II regions for these galaxies are shown in Figure 3.

1. We derive the internal dust extinction of the observed galaxies from the Balmer series. We follow the methodology discussed in Henry et al. (2021) to fit the higher signal-to-noise ratio (S/N) Balmer line flux ratios (Hα/Hβ, Hγ/Hβ, Hδ/Hβ) with two parameters, i.e., the internal $E(B-V)$ and stellar absorption. The latter is a nuisance parameter, so its inclusion contributes to an accurate determination of the uncertainties on $E(B-V)$. We adopt the extinction law from Cardelli et al. (1989) and assume an electron temperature (T_e) of 10,000 K.[20] Two out of our eight galaxies (J0152–0431 and J0208–0401) have unphysical Balmer decrements in Hα/Hβ, which cannot be fitted simultaneously with the Hγ/Hβ and Hδ/Hβ ratios. Their Hα features from the SDSS spectra also look asymmetric or clipped, which has previously been found in the literature (e.g., J1248+4259 in Izotov et al. 2018b). We attribute this to systematic errors in the SDSS data processing pipelines. Therefore, for these two galaxies, we exclude Hα in the above fitting process. The best-fitted internal $E(B-V)$ values are shown in Table 5.

[20] The derived $E(B-V)$ is only slightly dependent on T_e. For example, adopting $T_e = 15{,}000$ K will increase the derived $E(B-V)$ by only $\sim$0.02.

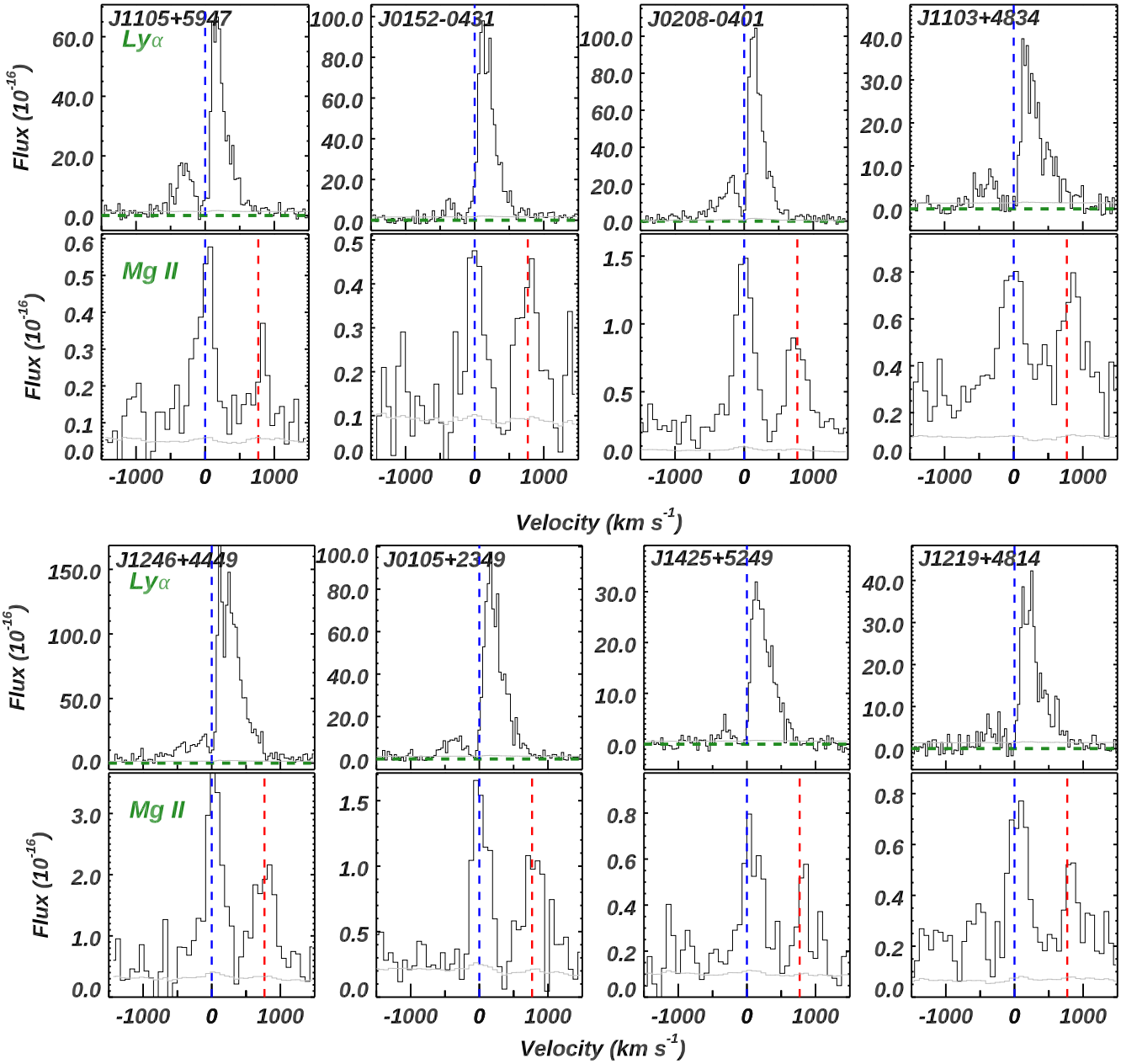

Figure 3. Comparisons of the observed Lyα and Mg II profiles in velocity space, with data taken from HST/COS and SDSS, respectively. The y-axes are in units of 10^{-16} erg s^{-1} cm^{-2} Å^{-1}. The data and corresponding errors are shown in black and gray. Objects are ordered by measured $f_{\rm esc}^{\rm LyC}$ in Section 3.1.1, while the last two objects have $f_{\rm esc}^{\rm LyC}$ as upper limits. The blue lines represent the $v = 0$ km s^{-1} for Lyα or Mg II λ2796, while the red lines represent $v = 0$ km s^{-1} for Mg II λ2803. The green dashed lines represent the positions of flux = 0 for Lyα panels.

2. Next, when measuring optical emission lines, we correct the SDSS spectra for both the MW and internal extinction, as well as the stellar absorption. After that, for lines of interest, we derive the continuum, measure the lines (i.e., flux, EW, and peak velocities), and calculate their errors adopting the same method discussed in Section 2.4. For the Mg II doublet, we divide the spectrum into two regions corresponding to each line, using the midpoint between the two lines, i.e., 2799.1 Å. Additionally, the Mg II line fluxes are not corrected for internal dust extinction, since a robust correction is difficult to discern when Mg II photons could be resonantly scattered like Lyα (e.g., Henry et al. 2018; Chisholm et al. 2020). We return to this question in Section 5.3.
3. For each galaxy, we compare the magnitudes from SDSS photometry in different bands (u, g, r, i, z) to the ones derived from SDSS spectra. Since our galaxies are compact (see Figure 1), these two sets of magnitudes are consistent for most of our galaxies. One exception is J1246+4449, where we scale the flux from its SDSS spectra by a factor of 1.29 to match its SDSS r-band magnitude. For other galaxies, we do not apply aperture corrections to their SDSS spectra.
4. We then derive electron density and temperature (n_e and T_e) and metallicity from optical emission lines using PyNeb (Luridiana et al. 2015). For n_e, since [O II]

Table 3
Measurements about Lyman Continuum

Object	$F(\mathrm{LyC})_B$[a] (E–17)	$F(\mathrm{LyC})_R$[a] (E–17)	$F(1100)$[b] (E–17)	$F(1300)$[b] (E–17)	$F(\mathrm{LyC})/F(1100)$[c] (%)	$F(\mathrm{LyC})/F(1300)$[c] (%)	$f_{\mathrm{esc}}^{\mathrm{LyC}}(\mathrm{H}\beta)$[d] (%)	$f_{\mathrm{esc}}^{\mathrm{LyC}}(\mathrm{SED})$[e] (%)
J0105+2349	$0.37^{+0.17}_{-0.15}$	NA	$12.00^{+0.43}_{-0.32}$	$9.9^{+0.62}_{-0.33}$	$3.1^{+1.4}_{-1.3}$	$3.7^{+1.7}_{-1.5}$	$1.2^{+0.8}_{-0.7}$	$0.7^{+0.3}_{-0.3}$
J0152–0431	<0.55	$1.69^{+0.54}_{-0.48}$	$8.71^{+1.91}_{-0.65}$	$10.37^{+0.97}_{-0.53}$	$19.4^{+6.4}_{-7.0}$	$16.3^{+5.4}_{-4.7}$	$8.6^{+4.7}_{-4.5}$	$9.8^{+3.1}_{-2.7}$
J0208–0401	$0.71^{+0.15}_{-0.13}$	$0.97^{+0.18}_{-0.17}$	$11.71^{+0.36}_{-0.28}$	$10.03^{+0.53}_{-0.31}$	$8.3^{+1.5}_{-1.5}$	$9.7^{+1.8}_{-1.7}$	$5.8^{+2.3}_{-2.2}$	$5.3^{+1.0}_{-0.9}$
J1103+4834	<0.41	$0.38^{+0.18}_{-0.16}$	$15.43^{+1.1}_{-0.62}$	$11.64^{+2.36}_{-0.76}$	$2.5^{+1.2}_{-1.1}$	$3.3^{+1.7}_{-1.4}$	$1.3^{+0.8}_{-0.8}$	$2.5^{+1.2}_{-1.0}$
J1105+5947	$0.65^{+0.24}_{-0.20}$	$1.37^{+0.21}_{-0.19}$	$10.07^{+0.78}_{-0.45}$	$7.28^{+1.68}_{-0.51}$	$13.6^{+2.2}_{-2.2}$	$18.8^{+5.2}_{-2.9}$	$13.0^{+6.1}_{-6.0}$	$13.6^{+2.1}_{-1.9}$
J1219+4814	<0.41	<0.30	$10.62^{+0.93}_{-0.51}$	$8.92^{+2.74}_{-0.76}$	<2.8	<3.4	<1.4	<1.3
J1246+4449([f])	$0.52^{+0.30}_{-0.29}$	NA	$32.86^{+1.14}_{-0.84}$	$25.42^{+1.5}_{-0.8}$	$1.6^{+0.9}_{-0.9}$	$2.0^{+1.2}_{-1.1}$	$1.1^{+0.8}_{-0.8}$	$0.8^{+0.5}_{-0.5}$
J1425+5249	<0.28	<0.28	$7.66^{+0.57}_{-0.34}$	$6.21^{+1.05}_{-0.39}$	<3.7	<4.5	<2.4	<2.3

Notes.
[a] The measured LyC flux density in units of 10^{-17} erg s^{-1} cm^{-2} Å^{-1}. $F(\mathrm{LyC})_B$ and $F(\mathrm{LyC})_R$ represent LyC flux measured at the blue and red side of geocoronal Lyα, respectively (see Figure 2 and Section 2.3.1). The final adopted $F(\mathrm{LyC})$ are shown in boldface. For J0105+2349 and J1246+4449, their Lyman limit is < 1250 Å (in observed frame). Therefore, they do not have $F(\mathrm{LyC})_R$ reported. For $F(\mathrm{LyC})$ that are consistent with zero, a 2σ upper limit is reported.
[b] The continuum flux measured around 1100 and 1300 Å, which are corrected by MW dust extinction but not by the internal extinction of the galaxy.
[c] The flux ratio of LyC to the continuum at around 1100 and 1300 Å.
[d] The absolute escape fraction of LyC from the Hβ method (see Section 3.1.2).
[e] The absolute escape fraction of LyC from the SED fitting method (see Section 3.1.1).
[f] J1246+4449 is also analyzed in LzLCS (Flury et al. 2022a). They reported $f_{\mathrm{esc}}^{\mathrm{LyC}}(\mathrm{H}\beta) = 0.9^{+0.5}_{-0.4}$ and $f_{\mathrm{esc}}^{\mathrm{LyC}}(\mathrm{SED}) = 0.5^{+1.0}_{-0.2}$, which are consistent with our values within error bars.

$\lambda\lambda$3727, 3729 are not resolved in SDSS spectra and the [S II] $\lambda\lambda$6716, 6731 doublet usually has low S/N, we assume $n_e = 100$ cm^{-3} as a characteristic of GP galaxies that show strong Mg II emission (Henry et al. 2018). For T_e, we use [O III] λ4363 along with [O III] $\lambda\lambda$4959, 5007 lines to determine T[O III], while T[O II] is scaled from T[O III] as discussed in Andrews & Martini (2013). Given n_e and T_e for each galaxy, we adopt the direct method using PyNeb to calculate $\mathrm{O}^{++}/\mathrm{H}^{+}$ ionic abundance from the intensity ratio of [O III] (λ4959 + λ5007)/Hβ, and $\mathrm{O}^{+}/\mathrm{H}^{+}$ ionic abundance from [O II] λ3727/Hβ. We then add them to obtain the total oxygen abundance, which is listed in Table 5.

3. Analysis

In this section, we focus on measuring three different absolute escape fractions (f_{esc}) for galaxies in our sample. We first estimate the LyC escape fractions ($f_{\mathrm{esc}}^{\mathrm{LyC}}$) from two different methods in Section 3.1. Then, we determine the Mg II escape fractions ($f_{\mathrm{esc}}^{\mathrm{MgII}}$) from CLOUDY models in Section 3.2. Finally, we derive the Lyα escape fractions ($f_{\mathrm{esc}}^{\mathrm{Ly}\alpha}$) in Section 3.3. We study possible correlations between these escape fractions in Section 4.

3.1. Determining LyC Escape Fractions

In the literature, two main methods have been adopted to infer the intrinsic LyC fluxes that, when compared to observations, give $f_{\mathrm{esc}}^{\mathrm{LyC}}$: (1) estimating the intrinsic LyC flux from from spectral energy distribution (SED) fitting (e.g., Izotov et al. 2021), and (2) estimating it from Hβ emission lines (e.g., Izotov et al. 2016a). We adopt these two methods and discuss them in detail below. In Section 3.1.3, we compare the derived $f_{\mathrm{esc}}^{\mathrm{LyC}}$ values with the flux ratio between the nonionizing continuum and LyC (e.g., Flury et al. 2022b), which is sometimes referred to as another proxy for $f_{\mathrm{esc}}^{\mathrm{LyC}}$.

3.1.1. Determining $f_{\mathrm{esc}}^{\mathrm{LyC}}$ from SED Fitting

To fit the SEDs, we adopt the Binary Population and Spectral Synthesis (BPASS) models (version 2.2.1; Stanway & Eldridge 2018), which include binary star populations. Comparing to other standard models such as Starburst99 (Leitherer et al. 1999), BPASS has been suggested to better represent both the local and high-z galaxies (e.g., Steidel et al. 2016). We use the Prospector spectra fitting code, which can take spectroscopic data from the UV to far-IR rigorously using a flexible spectroscopic calibration model (Johnson et al. 2021). Currently, the only BPASS model available within Prospector is the "-bin-imf135all_100" model, i.e., assuming a Salpeter initial mass function[21] (IMF; Salpeter 1955) with lower and upper mass cutoffs of 0.1 and 100 $M_{\odot}$, respectively, and the slope $\alpha = -2.35$. In the remainder of the paper, a BPASS SED specifically stands for this model.

We fit the extinction-corrected G140L data from HST/COS for each galaxy. We adopt the nonparametric star formation history model from Prospector, which assumes that SFR is constant within each of a user-defined set of temporal age bins. There are four parameters, i.e., total stellar mass over all ages, stellar metallicity, stellar dust attenuation, and the age bins. For each galaxy, the total stellar mass varies between 10^8 and $10^{10.5}$ $M_{\odot}$ with a step size of 0.05 dex, metallicity varies $\pm$ 0.3 dex around the measured abundance from optical emission lines in Section 2.5 with a step size of 0.02 dex, and stellar dust optical depth varies between 0.1 and 1.0 (at 5500 Å; see Conroy et al. 2009) with a step size of 0.05 dex. We adopt age bins of [0.0, 6.5], [6.5, 7.0], [7.0, 7.5], [7.5, 8.0], [8.0, 9.0], and [9.0, 10.0], where each pair represents the lower and upper look-back time in units of log(years). We assume the dust extinction law of Calzetti et al. (2000). We have also tested

[21] While a Salpeter IMF is only valid to ~0.4 $M_{\odot}$ and extrapolation will result in overestimated stellar masses relative to newer IMFs in, e.g., Chabrier (2003), this does not impact our UV-only fits later, which are dominated by the high-mass stars.

Table 4
Measurements about Lyα Emission Lines

Object	$F(\mathrm{Ly}\alpha)_B$[a] (E17)	$F(\mathrm{Ly}\alpha)_R$[a] (E17)	$\mathrm{EW}(\mathrm{Ly}\alpha)_B$ (Å)	$\mathrm{EW}(\mathrm{Ly}\alpha)_R$ (Å)	v_B^{peak}[b] (km s^{-1})	v_R^{peak}[b] (km s^{-1})	$f_{\mathrm{esc}}^{\mathrm{Ly}\alpha}$[c]
J0105+2349	142 ± 9	1270 ± 12	16 ± 2	75 ± 15	–273 ± 17	166 ± 15	$0.22^{+0.02}_{-0.02}$
J0152–0431	80 ± 11	1326 ± 15	18 ± 4	131 ± 13	–367 ± 23	124 ± 11	$0.36^{+0.04}_{-0.04}$
J0208–0401	343 ± 6	1283 ± 10	25 ± 3	69 ± 10	–195 ± 10	169 ± 15	$0.43^{+0.04}_{-0.04}$
J1103+4834	77 ± 12	647 ± 16	3 ± 0.4	22 ± 5	–347 ± 20	133 ± 12	$0.13^{+0.01}_{-0.01}$
J1105+5947	221 ± 11	805 ± 12	24 ± 2	55 ± 8	–341 ± 19	175 ± 16	$0.59^{+0.06}_{-0.06}$
J1219+4814	74 ± 10	667 ± 15	24 ± 2	95 ± 13	–226 ± 14	252 ± 23	$0.18^{+0.02}_{-0.02}$
J1246+4449	280 ± 11	2119 ± 13	7 ± 1	39 ± 6	–90 ± 10	116 ± 11	$0.22^{+0.02}_{-0.02}$
J1425+5249	29 ± 5	572 ± 6	5 ± 0.8	82 ± 12	–322 ± 20	136 ± 12	$0.23^{+0.02}_{-0.02}$

Notes.
[a] The integrated Lyα flux in units of 10^{-17} erg s^{-1} cm^{-2}. The values have been corrected by MW dust extinction but not by the internal extinction of the galaxy. $F(\mathrm{Ly}\alpha)_B$ and $F(\mathrm{Ly}\alpha)_R$ represent Lyα flux of the blue and red peaks, respectively (see Figure 3 and Section 2.4).
[b] v_B^{peak} and v_R^{peak} represent the velocity of the blue and red peak of the observed Lyα profiles, respectively.
[c] The escape fraction of Lyα (see Section 3.3).

other dust extinction laws such as Cardelli et al. (1989) and only found minor differences on the fitted parameters.

Before the SED fitting, we mask out spectral regions ± 550 km s^{-1} around ISM absorption lines, strong emission lines of the galaxy, MW absorption lines, and geocoronal emission lines. A few exceptions include the following: (1) for Lyα of the galaxy, we mask out ± 1500 km s^{-1} to remove the contributions from wide Lyα emission; (2) for Lyα and O I λ1302 of the MW, we mask out ± 1500 km s^{-1} owing to broad absorption and strong geocoronal lines; and (3) we also mask regions with $\lambda < 1100$ Å or $\lambda > 1900$ Å in the observed frame owing to the decreasing throughput of the gratings.

We compare the final fitted SEDs with the observed spectra in Figure 4. The COS spectra are shown as gray lines. The internal dust-reddened and unreddened models are shown as red and blue lines, respectively. The unreddened models are then adopted to measure the intrinsic LyC flux (i.e., $F_{\mathrm{int}}(\mathrm{LyC})$) given the same windows as we use to measure the observed LyC flux ($F_{\mathrm{obs}}(\mathrm{LyC})$; see Section 2.3.1). Overall, our SED models fit the COS spectra well. We then calculate the absolute $f_{\mathrm{esc}}^{\mathrm{LyC}} = F_{\mathrm{obs}}(\mathrm{LyC})/F_{\mathrm{int}}(\mathrm{LyC})$, and the results are shown in the last column of Table 3.

For each of our galaxies, we also report the best-fitting stellar dust attenuation in Table 5. This SED-derived quantity is ~a factor of two compared with the nebular attenuation (derived in Section 2.5). This is consistent with what is suggested in Shivaei et al. (2020).

3.1.2. Determining $f_{\mathrm{esc}}^{\mathrm{LyC}}$ from Hβ Emission

The Hβ emission line can be used to estimate the intrinsic LyC emission, as it is a direct measure of the number of ionizing photons absorbed by H I. However, while the Hβ flux is proportional to the total number of ionizing photons, our LyC measurement is in a small wavelength window just shortward of 912 Å. Hence, the relationship between the Hβ flux and the intrinsic LyC flux at our wavelengths of interest depends on the slope of the hydrogen-ionizing spectrum, and thereby the age of the stellar population. Following Izotov et al. (2016b) and Flury et al. (2022a), we account for this age dependence using EW(Hβ), which shows a strong relationship with $F(\mathrm{H}\beta)/F(\mathrm{LyC})$ in stellar population models. Note that $F(\mathrm{LyC})$ is the modeled flux at 900 Å in the rest frame (Izotov et al. 2016b), which is close to our LyC measurement windows (see Figure 2).

We reproduce this relationship under different models as shown in Figure 5. Four different models from Starburst99 (Leitherer et al. 1999) are shown, given burst or continuous SFR and different rotation velocities of stars. The relationship adopted in Izotov et al. (2016b) is shown as the black line. We also present the relationships from two BPASS models with burst SFR, i.e., one with and another without binary stars. Most of the models are consistent (~10% difference) when $\mathrm{EW}(\mathrm{H}\beta) \gtrsim 80$ Å, but the trend given by BPASS models with binary stars deviates from other models at $\mathrm{EW}(\mathrm{H}\beta) < 80$ Å. This is because BPASS models with binary stars have harder ionizing spectra at older ages owing to the coevolution of binary stars (see Figure 38 in Eldridge et al. 2017). All SB99 models also deviate from BPASS ones at $\mathrm{EW}(\mathrm{H}\beta) \gtrsim 450$ Å, which suggest that SB99 models produce harder ionizing spectra for very young galaxies. Since all galaxies in our sample have $80\ \text{Å} \lesssim \mathrm{EW}(\mathrm{H}\beta) < 300$ Å (see red diamonds in Figure 5), our derived intrinsic flux of LyC (i.e., $F_{\mathrm{int}}(\mathrm{LyC})$) is only weakly dependent on the choice of models. Therefore, we take the relationship in Izotov et al. (2016b; black line) and get

$$f_{\mathrm{esc}}^{\mathrm{LyC}} = \frac{F_{\mathrm{obs}}(\mathrm{LyC})}{F_{\mathrm{obs}}(\mathrm{LyC}) + F_{\mathrm{int}}(\mathrm{LyC})}, \quad (1)$$

where $F_{\mathrm{int}}(\mathrm{LyC})$ is the intrinsic (i.e., absorbed) flux of LyC derived from the Hβ emission line and $F_{\mathrm{obs}}(\mathrm{LyC})$ is the observed (i.e., leaked) LyC flux.

Since the LyC photons that escape from the galaxy do not contribute to the Hβ emission line, the $F_{\mathrm{int}}(\mathrm{LyC})$ used in Equation (1) is only an initial estimate (e.g., Izotov et al. 2016b; Flury et al. 2022a). The observed Hβ EW that we compare to Figure 5 must be corrected to account for the ionizing photons that escape. Therefore, we solve $f_{\mathrm{esc}}^{\mathrm{LyC}}$ iteratively, i.e., using the initial estimate of $f_{\mathrm{esc}}^{\mathrm{LyC}}$ to correct EW(Hβ) and recompute $f_{\mathrm{esc}}^{\mathrm{LyC}}$ until the solution converges. The corresponding errors are calculated from MC simulations, while we perturb the measured Hβ flux, EW, and observed LyC flux by their 1σ uncertainties and recalculate $f_{\mathrm{esc}}^{\mathrm{LyC}}$. The resulting $f_{\mathrm{esc}}^{\mathrm{LyC}}$ values and errors are shown in the second-to-last column of Table 3.

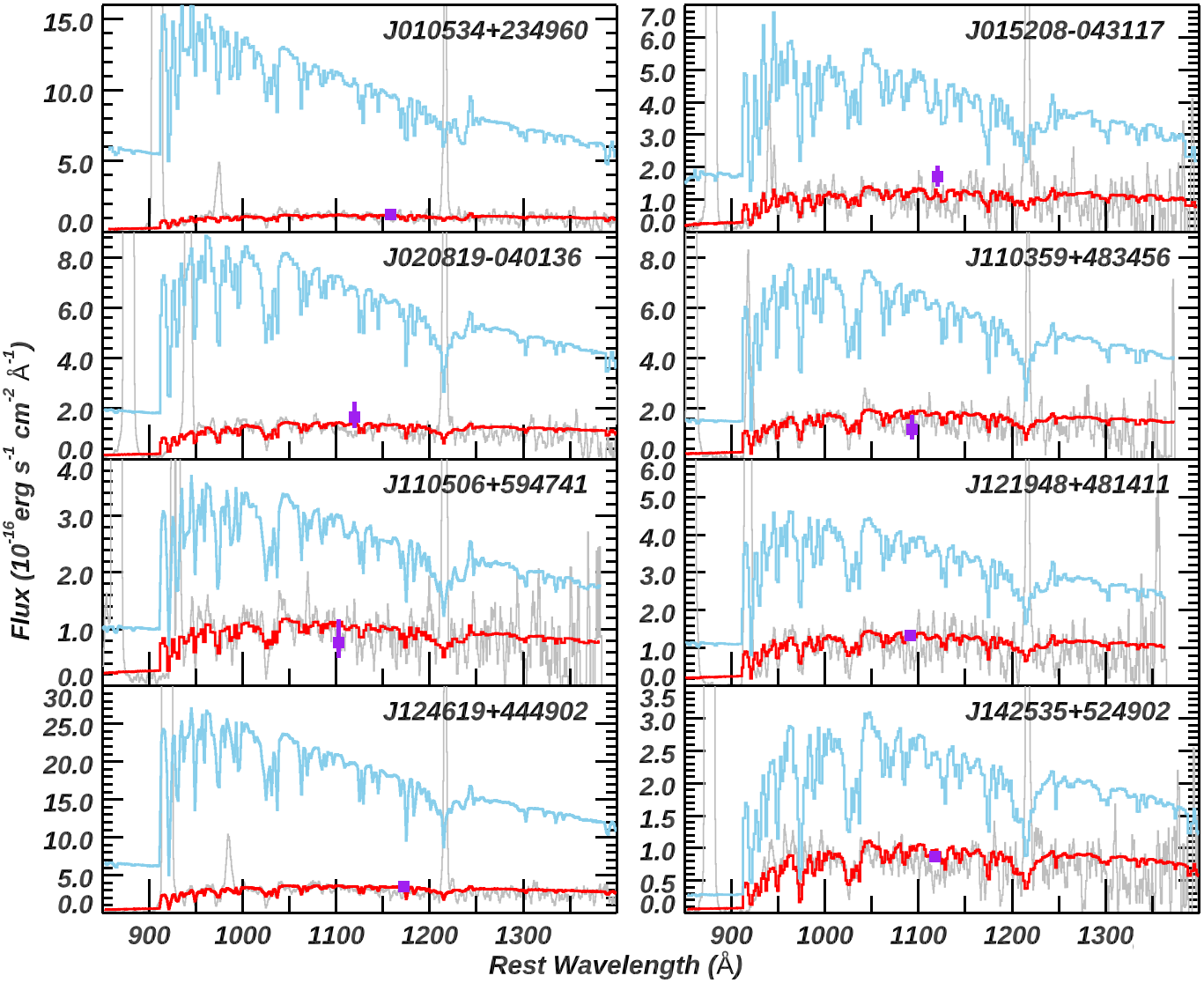

Figure 4. A comparison of the observed data and our best-fitting BPASS models. The COS G140L spectra are shown with gray lines, and photometric data from GALEX FUV are shown with purple squares. All data are dereddened by MW extinction (see Section 2.2). The red curves represent the BPASS models and are dereddened by only MW extinction. The blue curves are the models dereddened for both MW and internal extinction, which represents the intrinsic flux (see Section 3.1.1). We have resampled the data to bins of ∼2.5 Å to match the model's resolution.

3.1.3. Comparison of Different $f_{\rm esc}^{\rm LyC}$ Inferences

In the left panel of Figure 6, we compare the $f_{\rm esc}^{\rm LyC}$ results from the two methods in Sections 3.1.1 and 3.1.2. The $f_{\rm esc}^{\rm LyC}$ values with corresponding errors are shown as diamonds (or arrows for upper limits). We also calculate the Kendall's τ coefficient and the probability of the null hypothesis (p), where we take account of the upper limits following Akritas & Siebert (1996). These are shown in the upper left corner of each panel. The derived $f_{\rm esc}^{\rm LyC}$ values from the SED fitting and Hβ methods are consistent within 1σ, which enhances our confidence in the $f_{\rm esc}^{\rm LyC}$ measurements. This consistency also suggests that the dust destruction of LyC photons within HII regions is not substantial in our galaxies. Otherwise, LyC photons destroyed by dust would not contribute to the Hβ emission line and would cause the Hβ-derived $f_{\rm esc}^{\rm LyC}$ to be systematically higher than the SED-derived value.

Our galaxies' derived $f_{\rm esc}^{\rm LyC}$ values are ∼1%–14% in the cases where LyC is detected. In two of the galaxies, $f_{\rm esc}^{\rm LyC} \gtrsim 10\%$, which is significant compared to the values needed for galaxies in the EOR (5%–20%; e.g., Robertson et al. 2013; Rosdahl et al. 2018; Finkelstein et al. 2019; Naidu et al. 2020).

In the right panel of Figure 6, we also compare the derived $f_{\rm esc}^{\rm LyC}$ from SED fits to the ratio of ionizing to nonionizing UV continuum flux, i.e., $F_{\rm obs}({\rm LyC})/F(1300)$. The latter is a purely observational (model-independent) ratio. $F(1300)$ is the measured extinction-corrected flux at 1300 Å in the rest frame. We find that $f_{\rm esc}^{\rm LyC}$ positively correlates with $F_{\rm obs}({\rm LyC})/F(1300)$ for our galaxies. Note that it is not necessary to have $f_{\rm esc}^{\rm LyC} \simeq F_{\rm obs}({\rm LyC})/F(1300)$, since the latter is not a direct measurement of the LyC escape fraction (e.g., Flury et al. 2022a). We show $F_{\rm obs}({\rm LyC})/F(1300)$ and $F_{\rm obs}({\rm LyC})/F(1100)$ in Table 3.

3.2. Calculating Mg II Escape Fractions from CLOUDY Models

Previous studies have shown that photoionization models can be used to infer the escape fraction of Mg II ($f_{\rm esc}^{\rm MgII}$; e.g.,

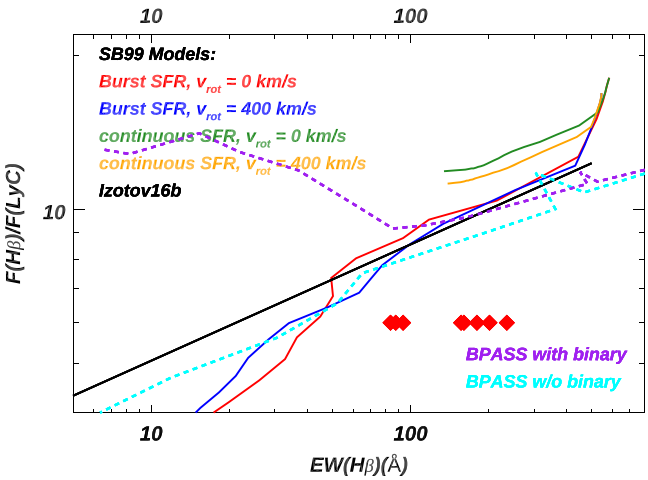

Figure 5. Comparisons of Hβ–LyC relationships between different stellar population models. F(LyC) is the model flux at 900 Å (rest frame). Models from Starburst99 (Leitherer et al. 1999) are listed in the upper left corner, where we choose either burst or continuous SFR with different rotation speeds. We show the fitted curve reported in Izotov et al. (2016b) as the black line. For BPASS models with burst SFRs, we show the cases with and without binary stars as purple and light-blue lines, respectively. Most of the models are consistent when EW(Hβ) $\gtrsim$ 80 Å, but the trend from BPASS models with binary stars deviates from other models at EW(Hβ) < 80 Å. Since all galaxies in our sample have EW(Hβ) > 80 Å (shown as the red diamonds at arbitrary y-positions), our derived intrinsic flux of LyC is only weakly dependent on the choice of models. See Section 3.1.2.

Guseva et al. 2013; Henry et al. 2018; Chisholm et al. 2020). By using multiple strong optical emission lines that are set by the ionization parameter, metallicity, density, and ionizing spectra, one can predict the intrinsic flux of Mg II ($F_{\rm int}$(Mg II)), which, combined with the observed flux of Mg II ($F_{\rm obs}$(Mg II)), gives the corresponding $f_{\rm esc}^{\rm MgII}$. However, previously published photoionization models for Mg II are only based on ionization-bounded (IB) cases, while models for density-bounded (DB) and mixed cases have not been studied in the literature. We briefly discuss these two cases below.

The mechanisms for Mg II, Lyα, and LyC photons (hereafter photons specifically stands for these three types) to escape from the galaxy are not fully understood. As discussed in the literature (e.g., Jaskot & Oey 2013; Zackrisson et al. 2013; Reddy et al. 2016b; Chisholm et al. 2020; Kakiichi & Gronke 2021), there are possibly two major scenarios: (1) Photons escape from DB cloud/nebulae. In this case, the cloud is smaller than its hydrogen Strömgren radius, and the intense radiation from massive stars ionizes all the gas in the cloud. Therefore, in this case photons can escape through optically thin gas (e.g., Chisholm et al. 2020). Alternatively, (2) photons escape through a clumpy geometry. In this case, most of the cloud remains neutral (i.e., IB) and is optically thick to escaping photons. Thus, photons escaping from these neutral paths suffer from intense scattering and are finally destroyed by dust. But there are low column density channels (possibly holes in ISM; e.g., Heckman et al. 2011; Saldana-Lopez et al. 2022) that allow photons to escape.

Recent observations of high detection rates of LyC escape from galaxies with high O32 values (e.g., Izotov et al. 2018b; Gazagnes et al. 2018; Ramambason et al. 2020; Izotov et al. 2021; Flury et al. 2022a; Saldana-Lopez et al. 2022) suggest that some clouds around those galaxies should be DB (i.e., covering fraction of DB clouds >0). Therefore, studies of photoionization models in DB cases are necessary. In Section 3.2.1, we first discuss the Mg II photon production in CLOUDY models. Then, in Section 3.2.2, we show the updated photoionization models to constrain $f_{\rm esc}^{\rm MgII}$ based on both DB and IB cases separately.

3.2.1. Mg II Photon Productions in CLOUDY Models

In Figure 7, we illustrate these two limiting cases of DB and IB by showing the physical structure of an ionized cloud that is at the transition between H I and H II zones. The vertical black line indicates the position of the hydrogen Strömgren radius, i.e., $\log(N_{\rm H}) = \log(U_{\rm H}) + 23.1$ (see Equation (3) in de Kool et al. 2002). We adopt the photoionization code CLOUDY (version c17.01; Ferland et al. 2017) with input parameters that are typical for galaxies in our sample. These include a BPASS SED with constant SFR and an age of 5 Myr, a stellar metallicity of $\log(Z_{\rm stars}/Z_\odot) = -1.5$ (assuming $Z_\odot = 0.02$), a gas-phase metallicity of $\log(Z_{\rm gas}/Z_\odot) = -1.5$, electron number density $\log(n_e) = 2.4$ (cm^{-3}), and ionization parameter $\log(U_{\rm H}) = -3.0$. The vertical axis represents the ion population for a certain element, e.g., n(O III) = the number of O III ions/total oxygen ions in all states. The horizontal axis is the total hydrogen column density (i.e., $N_{\rm H} = N$(H I) + N(H II)), which is a proxy for the depth into the cloud. The ionizing spectrum illuminates the cloud from the left.

If we truncate the CLOUDY model at radii far interior to the hydrogen Strömgren radius, the cloud is highly ionized and is analogous to a DB nebula. This limiting case is indicated by the red arrow in Figure 7. In this region, hydrogen is fully ionized, while the dominant form for oxygen is O III and n(Mg II) is ~10% of the total magnesium (red line in Figure 7). When we truncate the model at radii closer to (or after) the hydrogen Strömgren radius, the cloud transitions to be IB (see the blue arrow in Figure 7). The ions in this region change drastically from higher to lower or neutral ionization states, e.g., H II to H I and O III to O II. Additionally, n(Mg II) increases quickly near the IB region and becomes the dominant ion for magnesium when $N_{\rm H}$ is ~0.1 dex larger than at the Strömgren radius.

In the bottom panel of Figure 7, we show the accumulated log column density ($N_{\rm ion}$) of H I, Mg II O II, and O III from the CLOUDY model described above. For N(H I), we scale the curve down by 4.0 dex to include it in the figure. The horizontal orange line represents log N(H I) = 13.0 + 4.0 = 17.0 (cm^{-2}), where the cloud becomes optically thick to ionizing photons. From log N(H I) ~ 16.0 to 17.5, the curves of N(Mg II) and N(H I) are parallel (in red and black, respectively). This means that N(Mg II) can be adopted to trace N(H I) in a wide range of conditions from DB to IB regions (before the cloud is a lot deeper than the hydrogen Strömgren radius). This parallel in a wide range is because Mg II and H I are optically thin at similar $N_{\rm H}$ for our galaxies (results of metallicity, ionization potential, and oscillator strengths; see Chisholm et al. 2020).

We also find that the variations in metallicity or $\log(U_{\rm H})$ in the models only change the relative positions between the two curves or the positions of the hydrogen Strömgren radius. Therefore, our main conclusion in this subsection remains unchanged, i.e., the curves of Mg II and H I stay in parallel before hydrogen becomes mostly neutral.

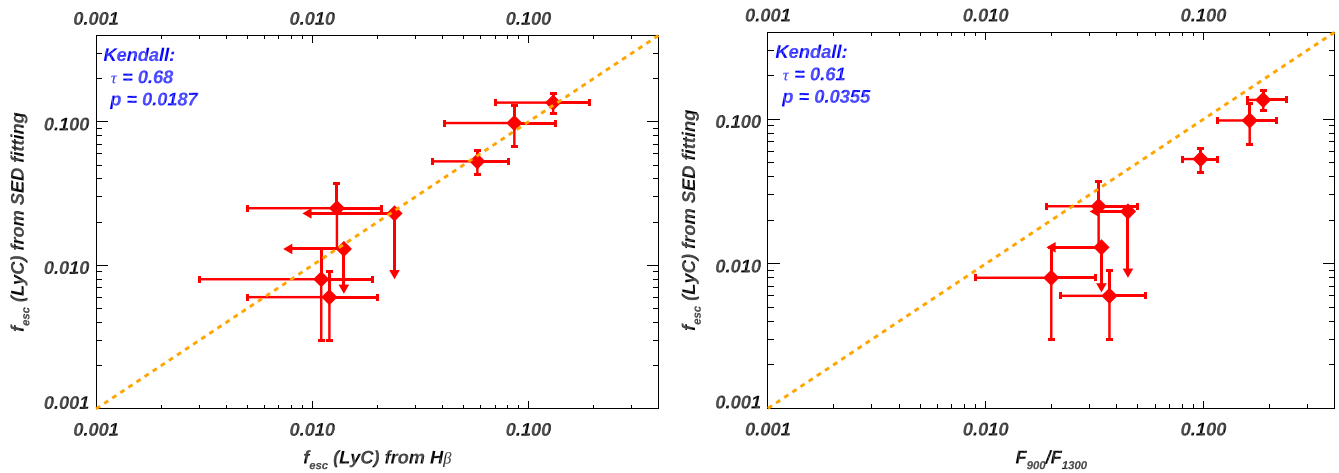

Figure 6. $f_{\rm esc}^{\rm LyC}$ measured from two different methods, and comparisons with UV continuum ratios measured at 900 and 1300 Å, respectively. Left: we compare the $f_{\rm esc}^{\rm LyC}$ values derived from SED fitting (Section 3.1.1) and the Hβ method (Section 3.1.2). Right: we compare the $f_{\rm esc}^{\rm LyC}$ values derived from SED fitting and UV continuum flux ratios ($F_{\rm obs}$(LyC)/F(1300)). For each figure, the Kendall's τ coefficient between the x and y values and the probability of the null hypothesis (p) are shown in the upper left corner. The objects with upper limits are denoted by the arrows, where we have taken account of these upper limits in the Kendall's τ test following Akritas & Siebert (1996).

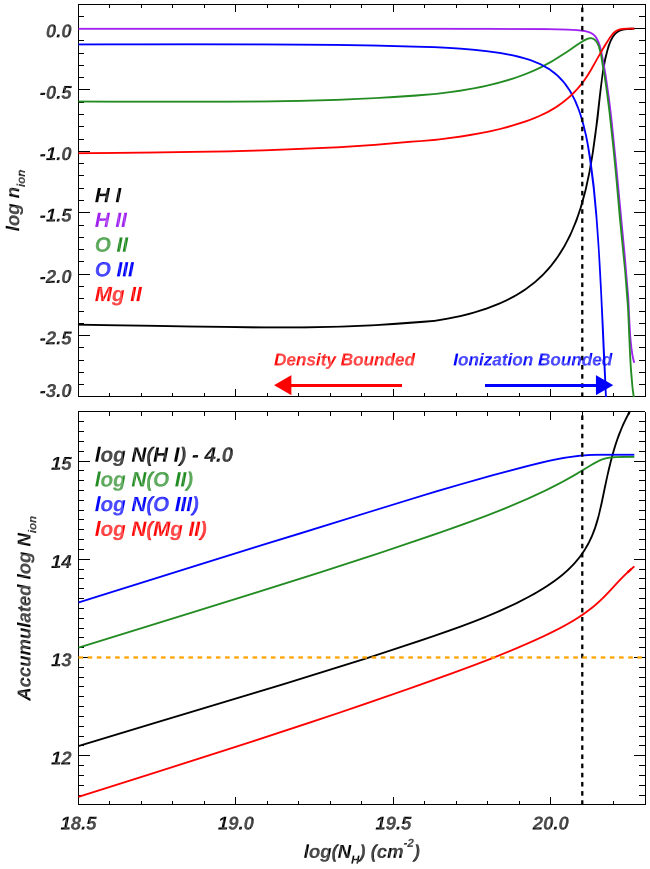

Figure 7. Physical structure of a photoionized cloud at the transition between H I and H II zones. Simulations are done using CLOUDY, and the adopted parameters are provided in Section 3.2.1. The position of the hydrogen Strömgren radius is indicated by the vertical black dashed line. The x-axis is the total hydrogen column density ($N_{\rm H}$). Top: comparison between $N_{\rm H}$ and the ion population for certain elements in the y-axis, e.g., n(O III) = the number of O III ions/total oxygen ions in all states. The approximated regions for the two limiting cases of density and ionization bounds are indicated by the two arrows separately. Bottom: accumulated $N_{\rm ion}$ for H I, O II, O III, and Mg II. For the curve of log(N(H I)), we scale it down by 4.0 dex to include it in the figure. The horizontal orange line represents N(H I) = 17.0 cm^{-2}, where the cloud becomes optically thick to ionizing photons (see discussion in Section 3.2.1).

3.2.2. Updated Mg II–O32 Correlations and $f_{\rm esc}^{\rm MgII}$

Henry et al. (2018) have determined a tight relationship to derive $F_{\rm int}$(MgII) from the extinction-corrected flux of [O III] λ5007 and [O II] λ3727 (see their Figure 4). Their models only considered the IB case in a slab geometry. However, various publications (e.g., Izotov et al. 2016a, 2016b, 2018a, 2018b, 2021; Flury et al. 2022a, 2022b) found higher detection rates of LyC escape from galaxies with increasing O32 values. This suggests that DB scenarios may be more prominent in LyC emitters (LCEs). Therefore, it is important to recalibrate the relationship considering both DB and IB cases.

We run grid models in CLOUDY, adopting the same SED, IMF, and log(n_e) as in Section 3.2 and Figure 7. We vary the stellar metallicity $Z_{\rm stars}$ = 0.001, 0.002, 0.004, 0.006, and 0.008; the gas-phase metallicity log($Z_{\rm gas}/Z_\odot$) = −1.5, −1.0, and −0.5; and the ionization parameter log($U_{\rm H}$) from −4.0 to −1.0 in steps of 0.1 dex. For DB, we stop the model at log($N_{\rm H}$) of 1.0 dex shallower than the hydrogen Strömgren layer, and for IB, we stop the model at log($N_{\rm H}$) of 0.1 dex deeper than the layer. Note that for these models with different metallicities, the abundance ratio of log(Mg/O) stays the same as the solar ratio in GASS10 (∼–1.1; see Grevesse et al. 2010). This is as expected since both magnesium and oxygen are alpha elements (created in core-collapse supernovae).[22]

An example of the correlation between Mg II and O32 is shown in Figure 8. Different colors are for models with different log($U_{\rm H}$) values. The circle and diamond symbols are for the DB and IB cases, respectively. Each color has a set of five symbols that stand for models with five different $Z_{\rm stars}$ values. The two black dashed lines represent the envelopes for all models for the full range of log($U_{\rm H}$) and $Z_{\rm stars}$. The solid red line is the fitted correlation in Equation (1) of Henry et al. (2018), which matches our dispersion well. Overall, different models from DB and IB only move the Mg II–O32 correlations along the line. This leads to one important advantage of the correlation, i.e., it is robust without any knowledge about the

[22] If magnesium is more heavily depleted onto dust than oxygen, the constant Mg/O ratio might not be a good assumption. But Henry et al. (2018) showed that this was not a big concern.

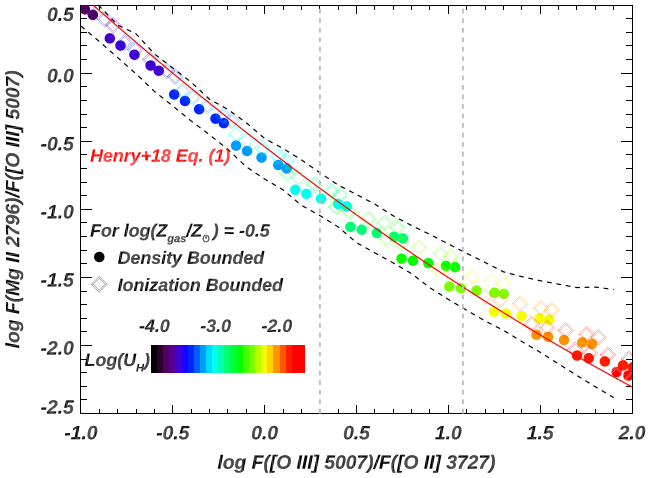

Figure 8. The tight correlation between the flux ratios of Mg II $\lambda2796$/[O III] and O32, which is based on the grid models from CLOUDY simulations. The input parameters are discussed in Section 3.2.1. Different colors are for different ionization parameters ($\log(U_{\rm H})$). The circles and diamonds are for the DB and IB cases, respectively. Each grid point (i.e., at certain $\log(U_{\rm H})$ and gas-phase metallicity) is plotted for five stellar metallicities ($Z_{\rm stars}$ = 0.001, 0.002, 0.004, 0.006, and 0.008). In these models, higher $\log(U_{\rm H})$ at lower stellar metallicities moves the line ratios downward along the sequence. The two black dashed lines represent the envelopes for all grid models varying $\log(U_{\rm H})$ and $Z_{\rm stars}$. The solid red line indicates the polynomial fits from Henry et al. (2018), which matches our correlations well. The galaxies discussed in this paper have O32 falling between the two gray vertical lines. This correlation for Mg II $\lambda2803$ has the same trend but differs by a factor of about 2. See details in Section 3.2.1.

actual limiting scenarios (either DB or IB or mixed) of the observed galaxy.

Figure 8 demonstrates that, given the observed extinction-corrected flux of [O III] $\lambda5007$ and [O II] 3727, we can predict the intrinsic flux ratio of Mg II/[O III] $\lambda5007$. We conduct polynomial fits to our full set of BPASS grid models under each $\log(Z_{\rm gas}/Z_\odot)$ value similar to Equations (1)–(3) of Henry et al. (2018) as follows:

$$R_{2796}({\rm DB}) = A_2 \times {\rm O32}^2 + A_1 \times {\rm O32} + A_0,$$
$$R_{2796}({\rm IB}) = B_2 \times {\rm O32}^2 + B_1 \times {\rm O32} + B_0, \quad (2)$$

where

$$R_{2796} = \log(F({\rm Mg\ II}\ \lambda2796)/F([{\rm O\ III}]\ \lambda5007)),$$
$${\rm O32} = \log(F([{\rm O\ III}]\ \lambda5007)/F([{\rm O\ II}]\ \lambda3727)). \quad (3)$$

Similar formulae exist for Mg II $\lambda2803$. The fitted parameters for different metallicities are shown in Table 6. Note that these correlations work best for O32 $\lesssim$ 20 (Figure 8).

Finally, given the ratios of R_{2796} and R_{2803}, we derive the intrinsic flux of Mg II ($F_{\rm int}$(Mg II)), which then leads to the escape fraction of Mg II as $f_{\rm esc}^{\rm MgII} = F_{\rm obs}({\rm Mg\ II})/F_{\rm int}({\rm Mg\ II})$. For each galaxy, we choose the model that has the closest gas-phase metallicity to the value we measured in Section 2.5. In this calculation, the observed Mg II flux ($F_{\rm obs}$(Mg II)) is corrected for MW extinction (see Section 4.2; see also Henry et al. 2018; Chisholm et al. 2020). The derived $f_{\rm esc}^{\rm MgII}$ values for Mg II $\lambda2796$ are listed in Tables 6 and 7. Since we only have SDSS optical spectra, we do not report $f_{\rm esc}^{\rm MgII}$ for Mg II $\lambda2803$ owing to the relatively lower S/N. But in Figure 9, we compare $f_{\rm esc}^{\rm MgII}$ from both lines, and we discuss possible implications in Section 4.2.

We have also tested CLOUDY models given the BPASS SED with burst SFR instead of the constant SFR discussed above. The difference in the resulting relationship is smaller than 5%.

3.3. Determining Lyα Escape Fraction

We calculate $f_{\rm esc}^{\rm Ly\alpha}$ from the ratio of Lyα and Hβ flux. Similar to Mg II, Lyα flux is only corrected for MW extinction owing to the unknown resonant scattering, while Hβ flux is corrected by both MW and internal extinction of the observed galaxy. We assume case B with an intrinsic Lyα/Hβ ratio of $\sim$23.3 under $T_{\rm e}$ = 10,000 K and n_e = 100 cm^{-3} (see Storey & Hummer 1995). We do not use the stronger Hα emission lines because of the clipping issues observed for some of the Hα emission lines (see Section 2.5 and Flury et al. 2022a). The resulting values are shown in Table 4.

4. Results

The observations that we have presented thus far show that at least 50% (four out of eight) of Mg II selected galaxies present LyC emission at 2σ significance, and derived $f_{\rm esc}^{\rm LyC}$ values range from $\sim$1.5% to 14%. We now explore the relationship between Mg II, Lyα, and LyC, as we aim to build diagnostics that can be applied in EOR galaxies. In Section 4.1, we introduce several comparison samples to extend the dynamic range for the correlations. In Section 4.2, we compare $f_{\rm esc}^{\rm MgII}$ with various galaxy and line properties. In Section 4.3, we contrast $f_{\rm esc}^{\rm Ly\alpha}$ with Mg II and Lyα line properties. Finally, we discuss various indirect indicators of $f_{\rm esc}^{\rm LyC}$, while comparing our Mg II selected galaxies with the whole LzLCS sample, in Section 4.4.

4.1. Comparison Samples

In the remainder of this paper, we consider several comparison samples from the literature that focused on selecting LCE candidates. A subset of these galaxies have Mg II emission detected in their optical spectra, including from (1) LzLCS (Flury et al. 2022a), (2) Izotov et al. (2016a, 2016b, 2018a, 2018b, 2021), (3) Henry et al. (2018), (4) Guseva et al. (2020), and (5) Malkan & Malkan (2021). For these samples, since they are not selected by strong Mg II emission, we only choose galaxies that have Mg II $\lambda\lambda2796$, 2803 both detected with S/N >3. There are overlaps between the different samples, where the same object was observed in more than one of the studies listed above. In this case, we always adopt the one with higher S/N. Overall, 24 extra LCE candidates from the literature are selected. Basic information and Mg II measurements for these galaxies and the eight from the present sample (a total of 32) are listed in Tables 6 and 7.

For galaxies from Izotov et al. and LzLCS samples, optical spectra are from SDSS. To reduce systematic errors, we remeasure the optical lines adopting the same methodology as in Sections 2 and 3 to get $f_{\rm esc}^{\rm MgII}$. For objects in Henry et al. (2018) and Guseva et al. (2020), since they have higher-S/N optical data, we adopt their line measurements directly. For all comparison samples, we take the reported flux of Lyα and recalculate $f_{\rm esc}^{\rm Ly\alpha}$ as discussed in Section 3.3. For $f_{\rm esc}^{\rm LyC}$, we take the reported values from the literature directly, which are commonly based on similar SED fittings as we discussed in Section 3.1.1.

Table 5
Basic Measurements for Galaxies in Our Sample

Object (1)	O32 (2)	O/H (3)	$E(B-V)_{\rm neb}$ (4)	$E(B-V)_{\rm ste}$ (5)	F_{2796} (6)	F_{2803} (7)	$\rm EW_{2796}$ (8)	$\rm EW_{2803}$ (9)	$f_{\rm esc}^{\rm MgII}$(DB) (10)	$f_{\rm esc}^{\rm MgII}$(IB) (11)
J0105+2349	4.3	8.2	0.139	0.239	33.0 ± 6.0	30.3 ± 5.2	8.8 ± 1.6	8.8 ± 1.6	0.26 ± 0.05	0.21 ± 0.04
J0152–0431	3.8	8.3	0.082	0.151	12.7 ± 2.4	11.0 ± 2.6	8.6 ± 1.6	7.5 ± 1.8	0.16 ± 0.03	0.13 ± 0.03
J0208–0401	5.8	7.2	<1E-3	0.180	40.1 ± 2.2	20.3 ± 2.2	9.9 ± 0.6	5.2 ± 0.6	0.54 ± 0.03	0.51 ± 0.03
J1103+4834	2.8	8.0	0.258	0.149	33.6 ± 3.4	27.1 ± 3.2	9.2 ± 1.0	7.4 ± 0.8	0.23 ± 0.03	0.19 ± 0.02
J1105+5947	4.2	8.1	0.202	0.100	13.8 ± 1.6	5.7 ± 1.4	9.1 ± 1.0	4.1 ± 1.0	0.40 ± 0.05	0.32 ± 0.04
J1219+4814	2.6	8.1	0.232	0.130	20.3 ± 2.0	9.0 ± 2.4	6.6 ± 0.8	3.0 ± 0.8	0.20 ± 0.02	0.15 ± 0.02
J1246+4449[a]	3.7	7.7	0.110	0.124	70.6 ± 8.2	37.6 ± 6.8	8.7 ± 1.2	4.9 ± 0.8	0.30 ± 0.04	0.26 ± 0.03
J1425+5249	4.4	7.8	0.056	0.115	28.0 ± 3.0	16.2 ± 3.2	16.6 ± 2.0	8.9 ± 1.6	0.59 ± 0.07	0.51 ± 0.06

Notes. Measurements from the optical spectra galaxies from our sample. Column (2): [O III] λ5007/[O II] λ3727 flux ratios. Column (3): gas-phase metallicity in the form of 12+log(O/H). Column (4): the fitted dust extinction from nebular lines. Column (5): the stellar dust extinction from SED fits of HST/COS data. Columns (6) and (7): measured flux of Mg II $\lambda\lambda$2796, 2803 in units of 10^{-17} erg s^{-1} cm^{-2}, separately. These fluxes have been corrected for MW dust extinction but not for the dust internal extinction of the galaxy. Columns (8) and (9): rest-frame EWs in units of Å for Mg II $\lambda\lambda$2796, 2803, separately. Columns (10) and (11): escape fractions for Mg II λ2796 lines for DB and IB cases, separately, which are derived from the photoionization models in Section 3.2.2.
[a] J1246+4449 is also included in the LzLCS project (Flury et al. 2022a).

In all correlation figures later in this section, we calculate the Kendall's τ coefficients and the probability of a spurious correlation (p values). We show these values in the upper left corner of each figure. In the Kendall test, we have accounted for the upper limits (if any) following Akritas & Siebert (1996). For a significance level of $\alpha = 0.025$, the sample sizes of 8 and 32 require $\tau \gtrsim 0.64$ and 0.25, respectively, to reject the null hypothesis (i.e., there is no correlation between the x and y values).

4.2. Correlations for $f_{\rm esc}^{\rm MgII}$

We first compare the derived $f_{\rm esc}^{\rm MgII}$ from the two limiting cases of DB and IB and from the two lines of the Mg II doublet in Figure 9. Our sample is shown in red, while galaxies from literature are shown in gray. In the left panel, we show the ratio of $f_{\rm esc}^{\rm MgII}$ from DB to IB in the y-axis and $f_{\rm esc}^{\rm MgII}$ from IB in the x-axis. We find that the $f_{\rm esc}^{\rm MgII}$ values from DB are always slightly higher (~10%–20%) than the ones from IB. This is as expected from Figure 8 as follows. For each galaxy, the O32 value is fixed by the observation, and the predicted intrinsic flux of Mg II is lower in DB. Therefore, under the same observed flux of Mg II, we expect higher $f_{\rm esc}^{\rm MgII}$ for the DB case.

In the right panel of Figure 9, we show the $f_{\rm esc}^{\rm MgII}$ values from the two lines of the doublet, i.e., Mg II $\lambda\lambda$2796 and 2803, assuming DB. The oscillator strength ratio, and therefore the optical depth ratio between these two lines, is 2:1. However, since Mg II is a resonant line, this theoretical optical depth ratio between Mg II $\lambda\lambda$2796 and 2803 does not directly translate into different escape fractions (e.g., Henry et al. 2018; Chisholm et al. 2020). Instead, we find that most of the galaxies have $f_{\rm esc}^{\rm MgII}(2796) \sim f_{\rm esc}^{\rm MgII}(2803)$. This suggests that, in these cases, the resonant scattering of Mg II is not significant enough to cause λ2796 to have a lower escape fraction. In other words, these galaxies' observed Mg II photons most likely leak through optically thin paths/channels (possibly holes in ISM; see Chisholm et al. 2020; Saldana-Lopez et al. 2022). For $f_{\rm esc}^{\rm MgII} \gtrsim 0.4$, the trend in Figure 9 has more dispersion. We also take caution here since most of the Mg II observations for these galaxies are from SDSS spectra, and the S/N of Mg II λ2803 is always smaller than Mg II λ2796. Future deeper observations would shrink the error bars and clarify this trend. For all correlations later in this section, we focus on Mg II λ2796 from the DB case since (1) the higher-S/N line yields more robust relationships and (2) Mg II photons, as discussed above, most likely escape from DB paths, especially when $f_{\rm esc}^{\rm MgII}$ is not high.

Table 6
Fitted Parameters for the Mg II–O32 Correlations[a]

λ(Mg II)	Metal[b]	A_0	A_1	A_2	B_0	B_1	B_2
2796	−1.5	−0.52	−0.93	0.09	−0.45	−0.97	0.076
2796	−1.0	−0.55	−0.94	0.10	−0.46	−0.97	0.074
2796	−0.5	−0.61	−0.94	0.12	−0.49	−0.96	0.074
2803	−1.5	−0.81	−0.93	0.09	−0.75	−0.96	0.082
2803	−1.0	−0.84	−0.94	0.11	−0.76	−0.97	0.077
2803	−0.5	−0.91	−0.93	0.13	−0.79	−0.96	0.077

Notes.
[a] See definitions of parameters in Equations (2) and (3).
[b] The logarithm of gas-phase metallicity relative to solar metallicity, i.e., $\log(Z_{\rm gas}/Z_\odot)$.

We next compare $f_{\rm esc}^{\rm MgII}$ with different observed properties in Figure 10. These correlations are consistent with the ones reported in Henry et al. (2018, see their Figures 5 and 9), but we show them in a larger sample here. In the top left panel, we find that the galaxies with higher observed EW(Mg II) may have higher $f_{\rm esc}^{\rm MgII}$, although the relation shows large scatter. For the same $f_{\rm esc}^{\rm MgII}$, our galaxies (in red) tend to show stronger EW(Mg II) than the control sample (in gray). One explanation is that the intrinsic flux of Mg II is stronger for our galaxies since they were selected as strong Mg II emitters. In the top right panel, we show the positive correlations between $f_{\rm esc}^{\rm MgII}$ with O32 values. This may be as expected since $f_{\rm esc}^{\rm MgII}$ and O32 are both possible tracers for the escape of LyC. However, caution needs to be taken since $f_{\rm esc}^{\rm MgII}$ is also derived from O32.

In the bottom panel, we present a negative correlation that galaxies with higher internal extinction (derived in Section 2.5) tend to have lower $f_{\rm esc}^{\rm MgII}$. This is consistent with our expectations qualitatively, since the more dust, the fewer photons escape. Furthermore, we show the expectations from various extinction curves assuming no resonant scattering (e.g., Cardelli et al. 1989; Calzetti et al. 2000; Reddy et al. 2016a). Since most of the galaxies in our combined sample fall below the extinction curves, we infer that Mg II is indeed more

Table 7
Measurements from Optical Spectra for the Comparison Sample

Object (1)	O32 (2)	O/H (3)	$E(B-V)_{\rm neb}$ (4)	F_{2796} (5)	F_{2803} (6)	$\rm EW_{2796}$ (7)	$\rm EW_{2803}$ (8)	$f_{\rm esc}^{\rm MgII}$(DB) (9)	$f_{\rm esc}^{\rm MgII}$(IB) (10)	Ref. (11)
J1152+3400	5.2	8.0	0.060	34.9 ± 5.0	26.6 ± 5.6	4.7 ± 0.6	3.9 ± 0.8	0.32 ± 0.05	0.27 ± 0.04	(1)
J1503+3644	6.2	8.0	0.091	48.8 ± 3.8	26.3 ± 3.2	9.8 ± 0.8	5.5 ± 0.8	0.37 ± 0.03	0.33 ± 0.03	(1)
J0232–0426	11.1	7.9	0.035	4.7 ± 1.0	4.6 ± 1.4	9.5 ± 1.8	8.4 ± 2.4	0.54 ± 0.12	0.51 ± 0.11	(1)
J1046+5827	4.4	8.0	0.035	19.1 ± 2.6	15.1 ± 2.6	6.7 ± 1.0	5.7 ± 1.0	0.51 ± 0.07	0.42 ± 0.06	(1)
J1355+1457	7.6	7.8	0.094	15.8 ± 2.4	10.6 ± 2.6	8.7 ± 1.4	5.6 ± 1.2	0.32 ± 0.05	0.29 ± 0.05	(1)
J0911+1831	1.8	7.9	0.170	55.0 ± 10.0	37.0 ± 8.0	2.9 ± 0.4	1.9 ± 0.3	0.22 ± 0.04	0.18 ± 0.04	(2)
J0926+4427	3.2	8.0	0.100	217.0 ± 34.0	122.0 ± 33.0	5.1 ± 0.5	2.9 ± 0.5	0.48 ± 0.08	0.41 ± 0.07	(2)
J1054+5238	2.5	8.2	0.080	84.0 ± 17.0	66.0 ± 11.0	3.0 ± 0.3	1.6 ± 0.2	0.24 ± 0.05	0.19 ± 0.04	(2)
J1219+1526	10.5	7.9	0.010	141.0 ± 20.0	86.0 ± 9.0	6.2 ± 0.5	3.7 ± 0.3	0.63 ± 0.10	0.58 ± 0.10	(2)
J1244+0216	3.6	8.1	0.070	106.0 ± 12.0	38.0 ± 9.0	4.4 ± 0.4	1.6 ± 0.3	0.23 ± 0.03	0.19 ± 0.03	(2)
J1249+1234	3.5	8.1	0.070	120.0 ± 5.0	71.0 ± 5.0	9.1 ± 0.4	5.3 ± 0.4	0.59 ± 0.05	0.47 ± 0.04	(2)
J1424+4217	6.2	8.0	0.040	180.0 ± 11.0	141.0 ± 9.0	5.4 ± 0.3	4.3 ± 0.3	0.43 ± 0.04	0.36 ± 0.04	(2)
J0122+0520	5.6	7.9	<1E-3	34.2 ± 4.2	20.4 ± 4.2	7.2 ± 0.8	4.9 ± 0.8	0.77 ± 0.10	0.68 ± 0.09	(3)
J1326+4218	3.3	8.2	0.166	52.4 ± 9.2	27.7 ± 7.8	6.5 ± 1.0	3.2 ± 1.0	0.25 ± 0.04	0.20 ± 0.04	(3)
J0047+0154	3.4	8.1	0.169	39.6 ± 4.0	16.5 ± 3.4	4.4 ± 0.4	1.9 ± 0.4	0.27 ± 0.03	0.22 ± 0.02	(3)
J1246+4449	3.4	8.0	0.157	90.8 ± 10.6	44.9 ± 8.2	11.3 ± 1.4	6.0 ± 1.0	0.36 ± 0.04	0.29 ± 0.03	(3)
J1517+3705	2.4	8.3	0.196	37.0 ± 4.6	16.4 ± 4.4	6.2 ± 0.8	2.3 ± 0.6	0.17 ± 0.02	0.13 ± 0.02	(3)
J1648+4957	2.6	8.2	<1E-3	10.4 ± 3.0	11.9 ± 2.4	11.9 ± 3.2	11.2 ± 2.4	0.42 ± 0.12	0.33 ± 0.10	(3)
J1154+2443	11.6	7.6	0.049	12.2 ± 0.9	6.5 ± 0.9	6.1 ± 0.1	3.3 ± 0.1	0.60 ± 0.06	0.56 ± 0.05	(1,4)
J1442–0209	6.8	7.9	0.120	47.8 ± 2.6	25.1 ± 2.0	11.9 ± 0.2	6.4 ± 0.1	0.70 ± 0.05	0.63 ± 0.05	(4)
J0901+2119	7.7	8.2	0.129	17.5 ± 1.0	9.0 ± 0.7	10.7 ± 0.2	5.7 ± 0.1	0.48 ± 0.04	0.41 ± 0.03	(4)
J0925+1403	5.4	7.9	0.122	31.0 ± 1.9	15.5 ± 1.5	6.1 ± 0.1	3.1 ± 0.1	0.37 ± 0.03	0.33 ± 0.03	(4)
J1011+1947	28.8	8.0	0.094	8.0 ± 0.6	4.4 ± 0.5	5.0 ± 0.1	2.8 ± 0.1	0.39 ± 0.04	0.40 ± 0.04	(4)
J0207+0047	2.7	8.3	0.180	65.5 ± 4.4	40.9 ± 4.8	7.3 ± 0.4	4.5 ± 0.6	0.23 ± 0.02	0.18 ±0.01	(5)

Notes. Measurements from the optical spectra from published LCE candidates in the literature with high-S/N Mg II detections. The labels are the same as in Figure 6.
References: (1) Izotov et al. 2016a, 2016b, 2018a, 2018b, 2021; (2) Henry et al. 2018; (3) Flury et al. 2022a; (4) Guseva et al. 2020; (5) Malkan & Malkan 2021.

affected by dust than nonresonant lines. A similar relationship has also been found between Lyα and dust (see Figure 2 in Hayes et al. 2011).

The combination of the latter two panels also suggests that O32 may be correlated with the internal extinction. We indeed find a weak negative correlation between them, but there exist large scatters.

4.3. Correlations for $f_{\rm esc}^{\rm Ly\alpha}$

Since both Lyα and Mg II are scattered by low-ionization gas while they escape the galaxy, a direct correlation between their escape fractions has been suggested by a previous publication (Henry et al. 2018). We verify this correlation in our larger sample in Figure 11. The left panel shows the positive correlation between EW(Mg II λ2796) and EW(Lyα) but with moderate scattering. The right panel presents that $f_{\rm esc}^{\rm MgII}$ and $f_{\rm esc}^{\rm Ly\alpha}$ are tightly correlated, given the possibility of spurious correlations, $p \lesssim 10^{-3}$. The best-fitting linear correlation is

$$\begin{aligned} f_{\rm esc}^{\rm MgII} &= a + b \times f_{\rm esc}^{\rm Ly\alpha} \\ a &= 0.136 \pm 0.05 \\ b &= 0.725 \pm 0.10. \end{aligned} \quad (4)$$

Our correlation in Equation (4) is similar to Equation (5) in Henry et al. (2018). The $f_{\rm esc}^{\rm MgII}$ and $f_{\rm esc}^{\rm Ly\alpha}$ values are of the same order. This supports a scenario where Mg II and Lyα mainly escape from optically thin (or DB) holes in ISM (e.g., Gazagnes et al. 2018; Chisholm et al. 2020; Saldana-Lopez et al. 2022). In this case, Mg II and Lyα photons travel through similar path lengths (likely in a single flight) when they escape from the galaxy. Therefore, the excess dust extinction due to resonant scattering is similar for both lines. Note that this does not contradict the point that Mg II and Lyα still suffer more from dust extinction than nonresonant lines (Section 4.2). One explanation is that Mg II and Lyα photons still undergo some (few) scatterings, thus extending their path lengths and the susceptibility to dust destruction.

The optically thin Mg II emission line was also presented in Chisholm et al. (2020). They obtained Keck Cosmic Web Imager (KCWI) spatially resolved Mg II maps for one LyC leaker (J1503+3644). From the spatially resolved ratio of the high-S/N Mg II doublet lines, they conclude that Mg II is indeed optically thin in most regions. Similarly for our galaxies, future higher-resolution, higher-S/N spectra would reveal whether our observed Mg II emission lines are optically thin and determine whether the Mg II lines are broadened by resonant scattering. Overall, the correlation between $f_{\rm esc}^{\rm Ly\alpha}$ and $f_{\rm esc}^{\rm MgII}$ can add key constraints to the mechanisms that allow Mg II, Lyα, and LyC to escape.

Since $f_{\rm esc}^{\rm Ly\alpha}$ traces the H I column density and $f_{\rm esc}^{\rm MgII}$ traces the Mg II column density, one may expect that the residuals in the right panel of Figure 11 are related to the gas-phase metallicity. However, we have tested this hypothesis, and there exists large scatter. Given the current sample size and scatter, we could not confirm or rule out the hypothesized relationship.

4.4. Correlations for $f_{\rm esc}^{\rm LyC}$

Direct detections of LyC flux for high-redshift galaxies are difficult owing to neutral IGM attenuation. Therefore, exploring and verifying indirect indicators from local galaxies is essential to interpret the growing samples of EOR galaxies that will be detected with JWST and the upcoming Extremely Large Telescope (ELT). A detailed discussion of all known indirect

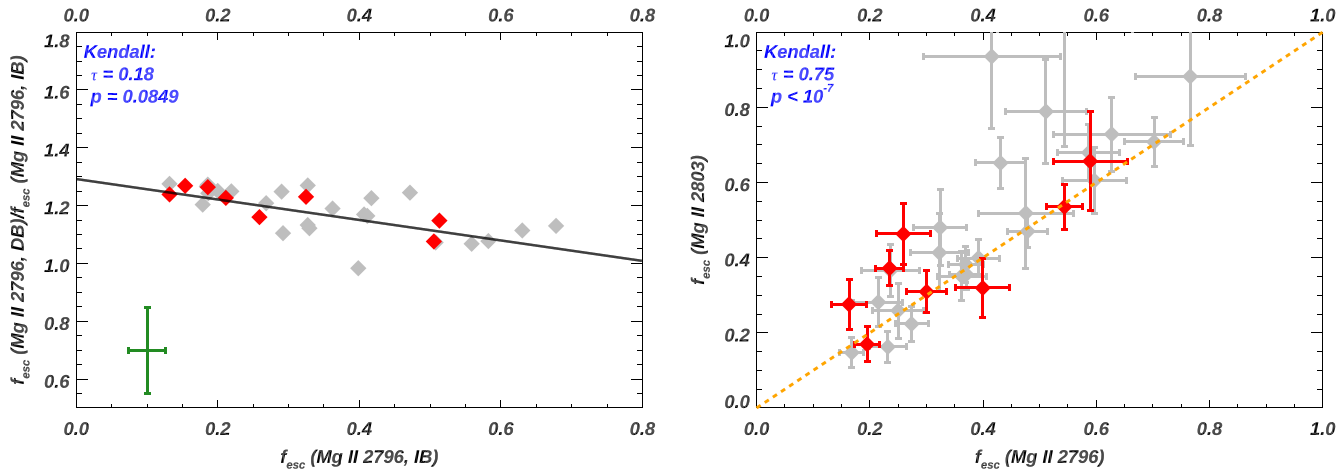

Figure 9. Comparison of the $f_{\rm esc}^{\rm MgII}$ values from the two limiting cases of DB and IB and two doublet lines. The eight galaxies in our sample are shown in red, while other possible LyC leakers from the literature with S/N of Mg II $\gtrsim 3$ are shown in gray (see Section 4.1). Left: the ratio of $f_{\rm esc}^{\rm MgII}$ from DB to IB vs. $f_{\rm esc}^{\rm MgII}$ from DB. We find general consistencies between the derived $f_{\rm esc}^{\rm MgII}$ values. But $f_{\rm esc}^{\rm MgII}$ from DB are always larger than the ones from IB as expected from the CLOUDY models (see discussion in Section 4.2). The black line represents the best linear fit, while the green cross represents the average error bar. Right: strong correlations between $f_{\rm esc}^{\rm MgII}$ from Mg II $\lambda\lambda$2796 and 2803, assuming DB. The scatter is mainly due to the low S/N for Mg II λ2803 emission line from SDSS spectra. For each figure, Kendall's τ coefficient and the probability of the null hypothesis (p) are shown in the upper left corner. The dashed lines represent the 1:1 relationship.

indicators in published LCE candidates has been presented in the Low-redshift Lyman Continuum Survey (LzLCS; see Flury et al. 2022b). In this subsection, we aim to contrast galaxies with high-S/N Mg II emission lines with all of the other LCEs (i.e., LyC leakers) and non-LCEs in the LzLCS. This survey contains 35 LCEs, but the majority have low-S/N (<3) detections of Mg II emission or completely lack spectroscopic coverage at the necessary blue wavelengths (~2800 Å in the rest frame).

In Figure 12, we compare the measured $f_{\rm esc}^{\rm LyC}$ to three possible indirect indicators, and we discuss the implications below. In all panels in Figure 12, our eight galaxies selected by strong Mg II emission are shown with red diamonds, while the other galaxies that have high-S/N Mg II emission are shown with dark-gray diamonds (see Section 4.1). In all panels, we also show galaxies from LzLCS that have low-S/N detections or nondetections of Mg II emission in gray circles. The open and filled circles indicate the LyC nonleakers and leakers, respectively. We have omitted the error bars for LzLCS samples to avoid crowding, but their error bars are comparable to the Mg II selected galaxies.

The correlation between $f_{\rm esc}^{\rm LyC}$ and O32 is shown in the first panel of Figure 12. A high O32 value has been proposed to be an indirect indicator of escaping LyC photons (e.g., Jaskot & Oey 2013; Nakajima & Ouchi 2014; Izotov et al. 2021; Flury et al. 2022b). It is evident that $f_{\rm esc}^{\rm LyC}$ increases with rising O32 values, and our Mg II selected galaxies (in red) fall into the same trend of all other galaxies. Consistent with previous publications (e.g., Izotov et al. 2021; Flury et al. 2022b), there still exists substantial scatter, which can be due to the dependence of O32 on other galaxy properties, e.g., metallicity, ionization, and geometry. Note that our eight galaxies show relatively low O32 values because they were not selected to have high O32. Izotov et al. (2021) also found in their sample very low $f_{\rm esc}^{\rm LyC}$ (<0.01) for galaxies with O32 < 4. However, in our combined sample, there are ~17 galaxies with O32 < 4 and $f_{\rm esc}^{\rm LyC} \gtrsim 0.01$. This subset is composed of our eight Mg II selected galaxies (red), along with nine from the LzLCS (gray circles). It is clear that for galaxies with 2 < O32 < 4 a moderate amount of ionizing photons (1%–10%) can still escape from the galaxies.

Another indirect indicator proposed in the literature is the profile of Lyα emission line. The peak separation ($V_{\rm sep}$) of the Lyα profile has been suggested to be one of the better proxies since it is sensitive to HI along the line of sight and can be directly measured from moderate- to high-resolution spectra (e.g., Dijkstra et al. 2016; Verhamme et al. 2017; Izotov et al. 2018b; Gazagnes et al. 2020; Kakiichi & Gronke 2021). In the second panel of Figure 12, we show the correlation between $f_{\rm esc}^{\rm LyC}$ and $V_{\rm sep}$. From the LzLCS sample, only seven galaxies have the HST/COS G160M observations needed for accurate measurements of $V_{\rm sep}$ (gray circles). While most of the galaxies follow the negative trend that has been suggested by previous publications (e.g., Verhamme et al. 2017; Izotov et al. 2018b, 2021; Flury et al. 2022b), a few of our objects are off. The largest deviation is for J1246+4449 at $V_{\rm sep}$ ~205 km s^{-1}. This could be because there are at least three peaks observed in J1246+4449's Lyα profiles (see Figure 3), instead of the commonly observed blue+red peak patterns. The two red peaks (at v >0) in J1246+4449 correspond to $V_{\rm sep}$ ~ 205 and 350 km s^{-1}. We therefore show the separation between the blue peak and each of these red peaks as red and green diamonds at $f_{\rm esc}^{\rm LyC} = 0.009$. We find that the wider $V_{\rm sep}$ (green) match better the negative trend between $f_{\rm esc}^{\rm LyC}$ and $V_{\rm sep}$. Similarly, other galaxies that may have >2 peaks in their Lyα profiles are J0105+2349 and J1219+4814 (see Figure 3).

This multiple-peak Lyα feature may be due to the two SF clumps in J1246+4449 (see its NUV image in Figure 1). In this case, its blue peak should also have two subpeaks. However, it is unclear owing to the low S/N on the blue peak in the COS spectrum. Overall, we caution that, in these cases, $V_{\rm sep}$ can be ill-defined and may affect the resulting trend with $f_{\rm esc}^{\rm LyC}$ (see similar cases in J1243+4646 in Izotov et al. 2018b; Rivera-Thorsen et al. 2019; Naidu et al. 2022).

For all galaxies, we also check their kinematics in optical emission lines. We find that they all show Gaussian-like profiles and only have one velocity center peaked at $v = 0$. Thus, there is no evidence that the observed optical emission-

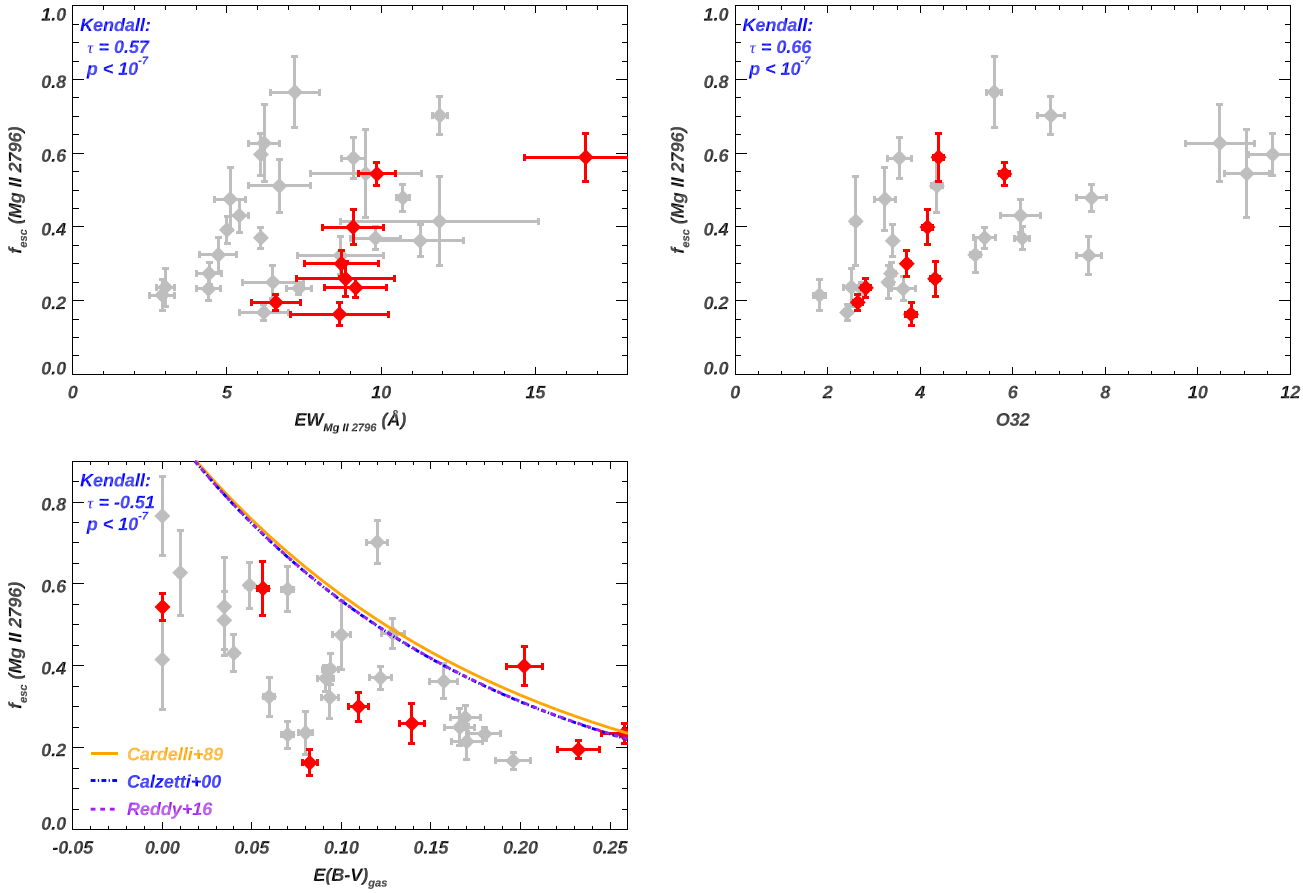

Figure 10. Comparisons of $f_{\rm esc}^{\rm MgII}$ (in y-axes) with EW of Mg II λ2796 (top left), O32 (top right), and the internal extinction of the observed galaxy (bottom). In the bottom panel, the dashed lines represent expectations from dust extinction laws without resonant scattering (note that Calzetti et al. 2000 and Reddy et al. 2016a curves mostly overlap). Colors and labels are similar to Figure 9. See discussion in Section 4.2.

line flux is from only one of the clumps. But we also note that the spectral resolution in SDSS may be insufficient to check the detailed kinematics.

In the third panel of Figure 12, we compare $f_{\rm esc}^{\rm LyC}$ with $f_{\rm esc}^{\rm Ly\alpha}$. Our galaxies selected by Mg II emission follow the same trend as other galaxies from LzLCS. The positive trend with moderate scatter is consistent with previous publications (e.g., Flury et al. 2022b).

4.5. Predicting $f_{\rm esc}^{\rm LyC}$ Using Mg II Emission Lines

As shown in Section 3.2.1 and Figure 7, given similar ionization potentials, N(Mg II) can be used to trace N(H I) in a large range from DB to nearly IB regions. Then, in Section 3.2.2, we showed how photoionization models can be used to infer $f_{\rm esc}^{\rm MgII}$ in both DB and IB regions. In this subsection, we aim to connect the observed Mg II emission and measured $f_{\rm esc}^{\rm MgII}$ to the escape of LyC. We adopt the methodology that was previously discussed in Chisholm et al. (2020), and we briefly summarize it as follows.

Mg II (or Lyα and LyC) escape in the two scenarios discussed in Section 3.2 can be generalized into one partial-covering geometry:

$$f_{\rm esc}\,({\rm Mg\ II}) = \frac{F_{\rm obs}}{F_{\rm int}} = (1 - C_f)e^{-\tau_{\rm thin}} + C_f e^{-\tau_{\rm thick}}, \qquad (5)$$

where $F_{\rm obs}$ and $F_{\rm int}$ are the observed and intrinsic flux of Mg II, respectively; C_f and $1 - C_f$ are the covering fractions for the IB and DB paths, respectively; and $\tau_{\rm thick}$ and $\tau_{\rm thin}$ are the optical depths for Mg II at IB (optically thick) and DB (optically thin) paths, respectively. This equation is valid for both Mg II $\lambda\lambda$2796 and 2803, where their optical depth ratios are related as $\tau_{2796} = 2\tau_{2803}$, given the ratio of their oscillator strengths.

For IB paths, we have $\tau_{\rm thick} \gg 1$, so photons cannot escape. Therefore, we can simplify Equation (5), and for Mg II λ2796

$$f_{\rm esc}\,({\rm Mg\ II\ 2796}) = (1 - C_f)e^{-\tau_{2796,\rm thin}}, \qquad (6)$$

where we assume that there is no dust in the DB paths (we discuss the effects of dust in Section 5.3). Chisholm et al. (2020) show that one can estimate $\tau_{\rm thin}$ from doublet line ratios in this geometry (see their Equations (19) and (20)) as

$$\frac{F_{2796,\rm obs}}{F_{2803,\rm obs}} = 2e^{-\tau_{2803,\rm thin}} = 2e^{-0.5\times\tau_{2796,\rm thin}}, \qquad (7)$$

where $\tau_{2796,\rm thin}$ and $\tau_{2803,\rm thin}$ are the optical depths for Mg II $\lambda\lambda$2796 and 2803 at the optically thin (DB) paths, respectively. For our eight galaxies, since their observed $F_{2796,\rm obs}/F_{2803,\rm obs} \geqslant 1.0$ (see Figure 3), we get $\tau_{2803,\rm thin} < -\ln(0.5) = 0.7$ or $\tau_{2796,\rm thin} < 1.4$. This means that all of our galaxies have (nearly) optically thin Mg II lines.

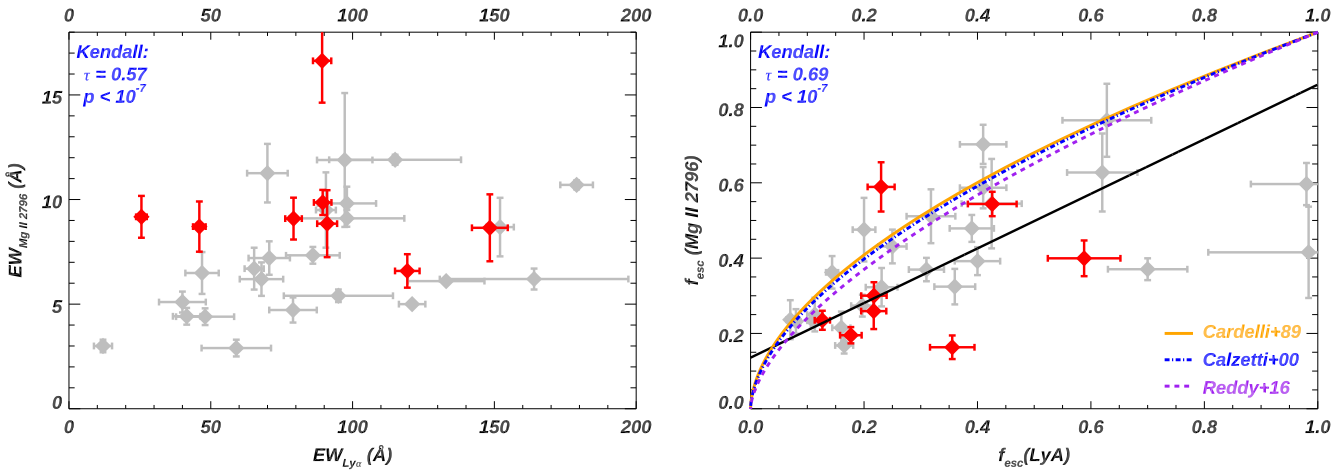

Figure 11. Correlations between Mg II and Lyα properties. Colors and labels are similar to Figure 9. Left: EW(Mg II λ2796) and EW(Lyα) are positively correlated. Right: the escape fractions of Mg II λ2796 and Lyα are tightly correlated. We show the expectations from different dust extinction laws *without* resonant scattering, and their references are in the lower right corner. The black line represents the best linear fit ($f_{\rm esc}^{\rm MgII} = 0.725 + 0.136\ f_{\rm esc}^{\rm Ly\alpha}$). See discussion in Section 4.3.

From the photoionization solutions discussed in Section 3.2.2, we have presented how to estimate $f_{\rm esc}$(Mg II 2796) given measured optical line flux. After that, we can solve the remaining two unknowns (C_f and $\tau_{2796,\rm thin}$) from Equations (6) and (7) given the observed flux of Mg II $\lambda\lambda$2796 and 2803 lines.

In Section 3.2.1, we have presented that N(Mg II) can be used to trace N(H I) in a wide range of conditions from DB to IB. Therefore, we get

$$N(\text{Mg II}) = \frac{3.8 \times 10^{14}}{f_{2796} \times 2796.35} \times \tau_{2796,\rm thin}\ (\text{cm}^{-2})$$
$$N(\text{H I}) = \alpha \times N(\text{Mg II}), \quad (8)$$

where $f_{2796} = 0.608$ is the oscillator strength of Mg II λ2796 and $\alpha = N(\text{Mg II})/N(\text{H I})$ is the column density ratio predicted from CLOUDY models in Section 3.2.1. For each galaxy, we have adopted their observed gas-phase metallicity and O32 to find the best-fit CLOUDY model. Finally, given the derived N(H I) from Equation (8), we can predict the absolute escape fraction of LyC (i.e., $f_{\rm esc,pd}^{\rm LyC}$) as

$$f_{\rm esc,pd}^{\rm LyC} = e^{-N(\text{H I})\sigma_{\rm ph}} \times 10^{-0.4E(B-V)k(912)}, \quad (9)$$

where the first term represents the absorption of LyC photons by neutral hydrogen and the second term stands for the stellar extinction by dust. Parameter $\sigma_{\rm ph}$ is the photoionization cross section of H I at 912 Å, and $E(B-V)\ k(912) = A(912)$, which is the total magnitude of extinction at 912 Å. From extinction laws in Cardelli et al. (1989), Calzetti et al. (2000), and Reddy et al. (2016b), $k(912) = 21.32$, 16.62, and 12.87, respectively. We adopt $k(912)$ from the Calzetti et al. (2000) extinction law to be consistent with our assumptions in the SED fittings in Section 3.1.1.

Given high enough S/N data on the required optical lines (i.e., Mg II $\lambda\lambda$2796, 2803, [O II] λ3727, and [O III] λ5007), one can solve Equations (6)–(9) to get $f_{\rm esc,pd}^{\rm LyC}$. However, it is difficult to do so in our eight galaxies and most of the other comparison galaxies discussed in Section 4.1. This is because, for most of these galaxies, their only optical spectra are from SDSS, where the observed Mg II has relatively low S/N, especially insufficient to solve Equation (7). Therefore, we assume $C_f = 0.0$, i.e., the Mg II photons all escape from DB paths. This was also adopted in Chisholm et al. (2020), where they confirmed it in one LCE, J1503+3644. Given this assumption, we can directly solve $\tau_{2796,\rm thin}$ from Equation (6), which then leads to $N_{\rm HI}$ and $f_{\rm esc,pd}^{\rm LyC}$ in Equations (8) and (9), respectively.

In Figure 13, we show the measured $f_{\rm esc}^{\rm LyC}$ derived from SED fitting vs. $f_{\rm esc,pd}^{\rm LyC}$ predicted from Mg II. We find a positive 1:1 correlation, which is consistent with the results in Chisholm et al. (2020). The rms error (RMSE) between the predicted and measured $f_{\rm esc}^{\rm LyC}$ is ~0.05. This suggests that the Mg II emission can be used to infer the LyC escape fraction when $f_{\rm esc}^{\rm LyC}$ is large (>5%). The scatter and moderate RMSE could be because our assumption of CF = 0.0 is not valid for some of these galaxies, especially when $f_{\rm esc}^{\rm LyC}$ is small. Those galaxies with very small $f_{\rm esc}^{\rm LyC}$ could have larger coverage of IB paths ($C_f \rightarrow 1$) instead of DB paths ($C_f \rightarrow 0$).

We caution that the derived $f_{\rm esc,pd}^{\rm LyC}$ in this way should only be considered rough estimates. In the future, we can reach more robust estimates of $f_{\rm esc,pd}^{\rm LyC}$ once we have higher-S/N optical spectra for these galaxies (X. Xu et al. 2022, in preparation).

5. Discussion

5.1. A High Detection Rate of LCEs in Mg II Emitters

As shown in Flury et al. (2022b), the detection rate of LCEs rises when the observed O32 increases. They consider galaxies with known LyC observations from various samples, including LzLCS, Izotov et al. (2016a, 2016b, 2018a, 2018b, 2021), and Wang et al. (2019). These galaxies are mainly selected by one or more of the following properties: high O32 values, high EW(Hβ), high SFR surface density, or a deficiency of [S II] emission. These studies conclude that, for galaxies with O32 > 10, the detection rates are >60%, while galaxies with 3 < O32 < 6 only have detection rates < 20%. For comparison, our galaxies are selected by strong Mg II emission with similar redshifts to the above samples. Given 3 < O32 < 6 for our eight galaxies (see Figure 12), our detection rate of LCEs is >50% (four out of eight, with two other tentative detections). This suggests that strong Mg II emitters might be more likely to leak LyC than similar galaxies without strong Mg II. This is as

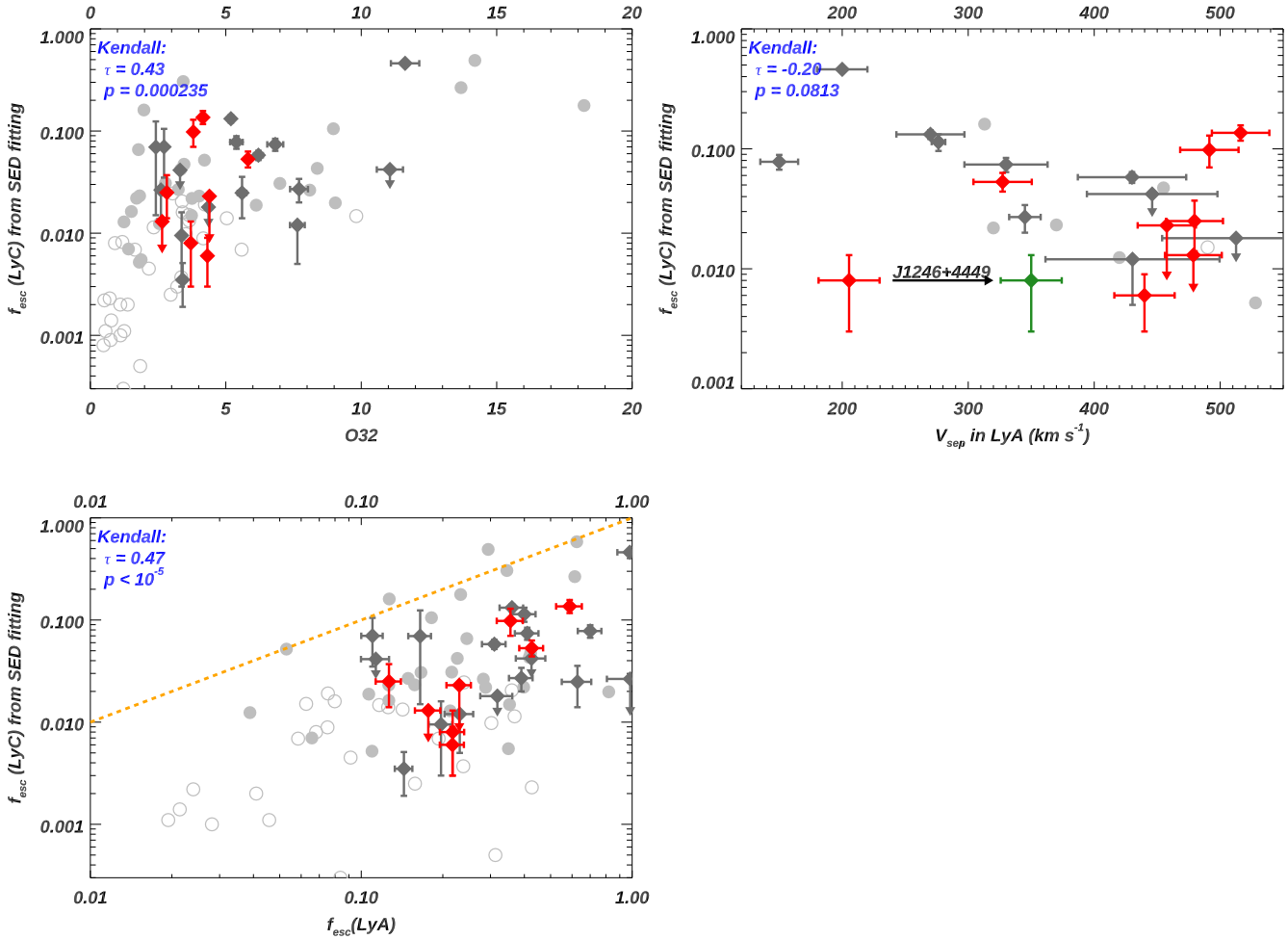

Figure 12. Relationships between the escape fraction of Lyman continuum ($f_{\rm esc}^{\rm LyC}$, in y-axes) and three possible indirect indicators (x-axes): (1) $f_{\rm esc}^{\rm LyC}$ vs. O32, (2) $f_{\rm esc}^{\rm LyC}$ vs. the peak separation of Lyα emission line ($V_{\rm sep}$), and (3) $f_{\rm esc}^{\rm LyC}$ vs. the escape fraction of Lyα. Galaxies from our Mg II selected sample are shown with red diamonds. Galaxies from comparison samples with high-S/N Mg II detections (Izotov et al. 2016a, 2018a, 2018b; Guseva et al. 2020; Izotov et al. 2021, and LzLCS) are shown with dark-gray diamonds. We also overlay other galaxies without high-S/N Mg II detections from the LzLCS sample. Their confirmed LyC leakers and nonleakers are shown with filled and open circles, respectively. In the right panel, galaxy J1246+4449 has two different $V_{\rm sep}$ (shown in red and green) owing to its triple-peak Lyα feature (see Section 4.4). In the bottom panel, we show where $y = x$ as the dashed orange lines.

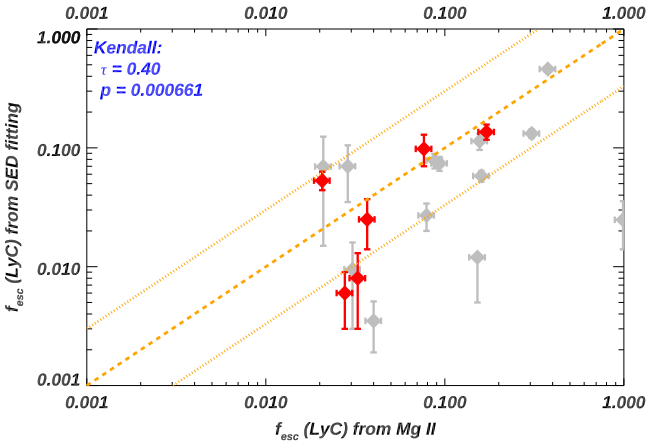

Figure 13. Comparisons of measured $f_{\rm esc}^{\rm LyC}$ with the predicted one from Mg II λ2796 emission lines and dust extinction (Section 4.5). Galaxies from our Mg II selected sample are shown with red diamonds, while galaxies from comparison samples with high-S/N Mg II detections (Izotov et al. 2016a, 2018a, 2018b; Guseva et al. 2020; Izotov et al. 2021; LzLCS) are shown with gray diamonds. We show where $y = x$ as the dashed orange lines and where $y = 1/3x$ and $3x$ as the dotted orange lines. There is a positive 1:1 correlation, and the RMSE is ∼0.05. See discussion in Section 4.5.

expected given that N(Mg II) traces N(H I) (see Section 3.2.1), and the observed $f_{\rm esc}^{\rm LyC}$ is positively related to $f_{\rm esc}^{\rm MgII}$ (see Section 4.5). Therefore, future large surveys of LCEs can consider Mg II as a constraint to gain higher efficiency in detections of LyC.

5.2. [S II] Deficiency in Mg II Emitters

Given the ionization potentials for creating and destroying [S II] of 10.4 and 23.3 eV, respectively, [S II] $\lambda\lambda$6716, 6731 would be weak or absent in an H II region that is optically thin to ionizing photons. Therefore, it has been proposed that [S II] deficiency is a probe of the optically thin cloud to LyC (e.g., Wang et al. 2019, 2021).

In Figure 14, we check the [S II] deficiency (defined below) for our combined sample of Mg II emitters and LzLCS galaxies. In the left panel, we compare intensity ratios of [O III]/Hβ with [S II]/Hα, while the orange line is the best-fitted correlation from SDSS DR12 SF galaxies (Wang et al. 2019). The colors and labels are similar to Figure 12, i.e., our eight galaxies are shown with red diamonds, the comparison samples that have high-S/N Mg II emissions are shown with

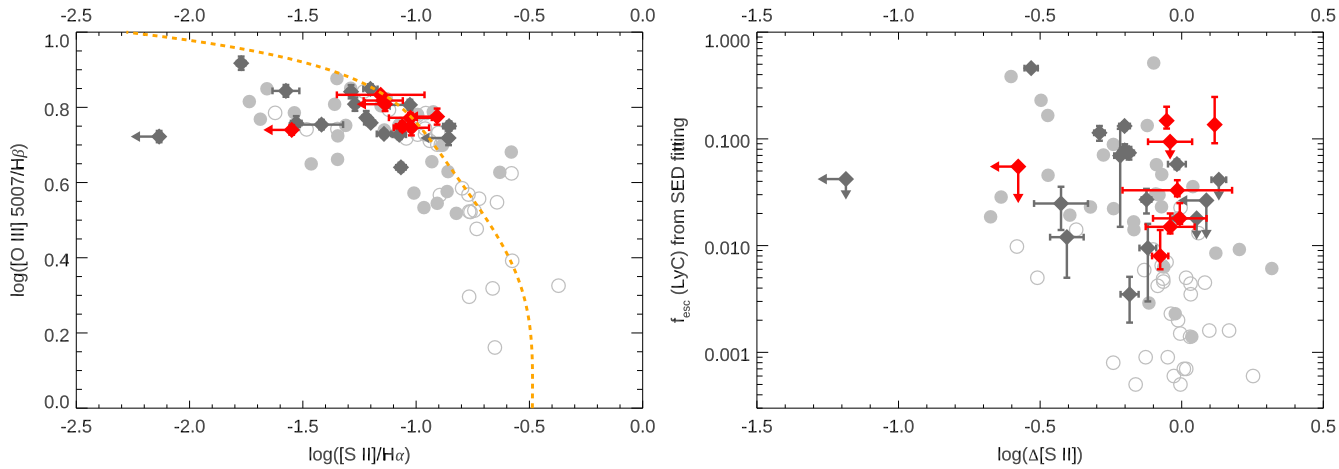

Figure 14. Correlations involving the deficiency of [S II] $\lambda\lambda$6716, 6731. The colors and labels are the same as in Figure 12. Left: we compare the flux ratios between [O III] λ5007/Hβ and [S II] $\lambda\lambda$6716, 6731/Hα. We show the fitted SDSS locus from Wang et al. (2019) as the orange line. Right: we compare the f_{esc}^{LyC} with [S II] deficiency. The latter is defined as the displacement of the measured log([S II]/Hα) from the orange line in the left panel (Wang et al. 2019, 2021). See discussion in Section 5.2.

dark-gray diamonds, and LzLCS galaxies are shown with circles. We find that galaxies with strong Mg II emission follow the same trend as the other LzLCS galaxies. In the right panel, we compare f_{esc}^{LyC} to the [S II] deficiency, which is defined as the displacement of the measured log([S II]/Hα) from the orange line in the left panel (Wang et al. 2019). The negative correlation has already been discussed in Wang et al. (2021), and the Mg II emitters are consistent with the same trend. This suggests that selecting objects with strong Mg II emission probes galaxies with similar [S II] deficiency to that in the LzLCS.

5.3. The Effects of Dust

Dust extinction plays important roles in the escape of Mg II. In the last panel of Figure 10, we have shown that Mg II is more affected by dust than nonresonant lines. In that figure, we do not correct the observed Mg II flux by internal dust extinction (of the observed galaxy) when calculating f_{esc}^{MgII} and adopting Mg II to predict f_{esc}^{LyC} above. This is because a robust correction is difficult to discern when Mg II photons could be resonantly scattered like Lyα (e.g., Henry et al. 2018; Chisholm et al. 2020). A quantitative assessment of the extinction in these resonant lines depends on how much scattering there is, which is tightly related to geometry, kinematics, H I column density, clumsiness, etc. (e.g., Neufeld 1990; Verhamme et al. 2006; Gronke et al. 2017), which is beyond the scope of this paper.

However, one interesting test is to treat Mg II as nonresonant lines and correct them by internal dust extinction similar to other optical lines. Since the observed Mg II lines in our sample should be close to optically thin (Section 4.5), this may be a fair first-order approximation. In Figure 15, we test this idea by remaking several correlations after correcting Mg II by internal dust extinction.

In the top panels of Figure 15, we compare f_{esc}^{MgII} to EW(Mg II) and O32, separately. As expected, the absolute value of f_{esc}^{MgII} for each galaxy increases compared to that of Figure 10. We also find that the resulting positive correlations in these two panels are similar (and slightly weaker) to those in Figure 10. For most galaxies, f_{esc}^{MgII} is still < 1.0 even though we have corrected Mg II by dust (top panels of Figure 15). This suggests that, for the majority of galaxies, the derived f_{esc}^{MgII} values cannot be explained purely by nonresonant scattering. This is consistent with what we show in the bottom panel of Figure 10 (see Section 4.2), where most galaxies fall below the prediction from dust extinction laws. Curiously, however, some galaxies have dust-corrected f_{esc}^{MgII} values >1.0. This could be because our chosen extinction law is inaccurate for these galaxies, or the $E(B-V)$ calculated from Balmer lines (Section 2.5) are too large for Mg II, or dust geometries are different (e.g., Scarlata et al. 2009).

In the bottom panel, we compare the measured f_{esc}^{LyC} from SED fits with the predicted f_{esc}^{LyC} from Mg II (see Section 4.5, but Mg II here has been corrected by internal dust). Notably, this figure is almost the same as Figure 13. This is as expected because we assume $C_f = 0.0$ in the calculations (see Section 4.5), i.e., the Mg II photons all escape from DB paths. In this case, the predicted f_{esc}^{LyC} from Equation (9) is insensitive to the change of optical depth of H I (which is correlated with N (Mg II) in Equation (8)).

6. Conclusion and Future Work

We have presented the analyses for eight LCE candidates selected with strong Mg II emission lines, i.e., EW(Mg II) $\gtrsim 10$ Å. These galaxies were observed with HST/COS G140L and G160M gratings (GO: 15865; PI: Henry) to cover their LyC and Lyα regions, respectively. These galaxies' Mg II emission lines have been observed in SDSS.

In 50% (four out of eight) of the galaxies, we securely detected LyC flux at $>2\sigma$ level. We determined the intrinsic flux of LyC from both SED fittings and Hβ emission lines, which are then adopted to predict the absolute LyC escape fraction (f_{esc}^{LyC}). We find that these two f_{esc}^{LyC} values are consistent with each other and fall within the range of $\sim$1%–14%.

We have discussed two geometries that allow Mg II (and Lyα, LyC) photons to escape in galaxies. By truncating CLOUDY models at different radii, we have shown that N (Mg II) can be used to trace N(H I) from DB to IB scenarios. To estimate the intrinsic flux of Mg II (which leads to f_{esc}^{MgII}), we have presented CLOUDY models under these two limiting scenarios, as well as the best-fit correlations. We highlight the

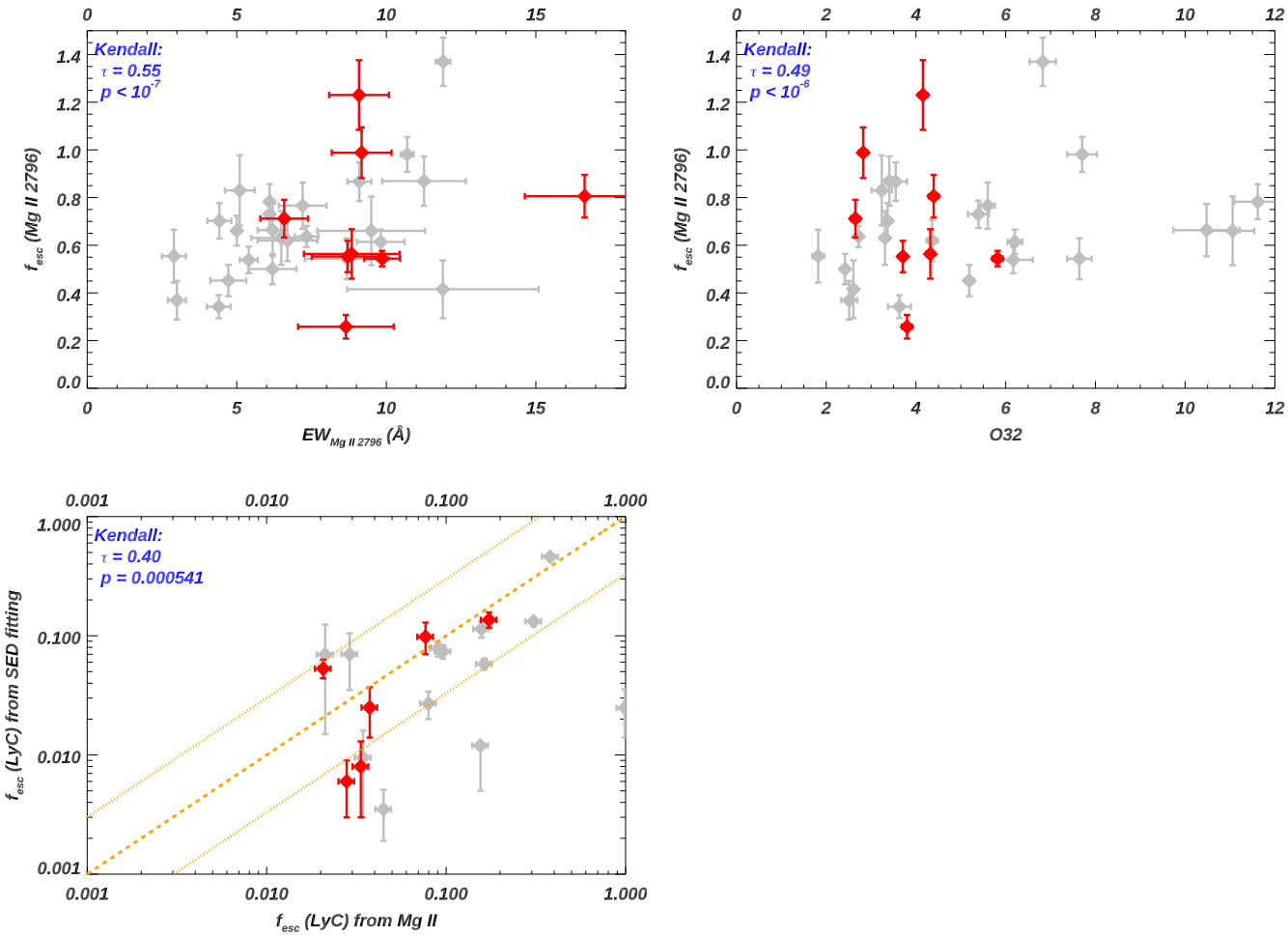

Figure 15. Same as Figures 10 and 13, but we now correct Mg II by nonresonant internal dust extinction of the observed galaxy. The correlations in these figures are similar to Figures 10 and 13. See discussion in Section 5.3.

fact that our derived $f_{\rm esc}^{\rm MgII}$ is insensitive to the prior knowledge of the limiting scenarios of the cloud around the galaxy.

We have built a larger comparison sample from published LCE candidates from the literature (Izotov et al. 2016a, 2016b, 2018a, 2018b; Henry et al. 2018; Guseva et al. 2020; Izotov et al. 2021; Malkan & Malkan 2021; Flury et al. 2022a). From them, we include 24 galaxies with high-S/N (>3) detections of Mg II emission lines. We find that our Mg II selected LCEs follow similar trends that have been established in the comparison sample. We show that $f_{\rm esc}^{\rm MgII}$ correlates positively with EW(Mg II) and O32, while moderate scatter exists for both correlations. Similar to Lyα, we find that $f_{\rm esc}^{\rm MgII}$ cannot be purely explained by dust extinction without resonant scattering. Furthermore, we study the correlation between Mg II and Lyα. We find that the measured EW and escape fractions from both lines are correlated, although with significant scatter. For the latter, the fact that $f_{\rm esc}^{\rm MgII}$ and $f_{\rm esc}^{\rm Ly\alpha}$ are of the same order is consistent with both lines escaping from DB optically thin holes in the ISM.

Finally, we have presented how to estimate $f_{\rm esc}^{\rm LyC}$ from the information of Mg II emission lines and dust extinction. This method works because we can trace N(H I) from N(Mg II) and then solve for the covering fraction of DB clouds from the Mg II $\lambda\lambda$2796, 2803 doublet. We find that the RMSE between the measured and predicted $f_{\rm esc}^{\rm LyC}$ is ~0.05. This suggests that the Mg II emission can be used to infer the LyC escape fraction when $f_{\rm esc}^{\rm LyC}$ is large (>5%). Future deeper observations of Mg II for more LCEs would shrink the scattering.

We have also noted that the detection rate of LCEs from our Mg II selected sample may be higher than from all other published LCEs *for galaxies with* $3 < O32 < 6$. Our high detection rate suggests that strong Mg II emitters might be more likely to leak LyC than similar galaxies without strong Mg II. Therefore, future large surveys can consider Mg II as a constraint to gain higher efficiency in detections of LyC.

There are various follow-ups to conduct in the future: (1) Consistent radiative transfer modeling of Lyα and Mg II (and LyC) could help to explain the current correlation that we find between $f_{\rm esc}^{\rm Ly\alpha}$ and $f_{\rm esc}^{\rm MgII}$ (and LyC). These correlations compared to dust extinction should also be related to the geometry of the ISM, which currently remains an open question. (2) Deeper and higher-resolution spectroscopic observations of the Mg II emitters than SDSS (e.g., from larger telescopes) would provide necessary information to predict $f_{\rm esc}^{\rm LyC}$ from Mg II. This would further test our proposed correlation between the predicted and measured $f_{\rm esc}^{\rm LyC}$. (3) Large infrared and optical telescopes, e.g., JWST and future ELT, can detect Mg II at higher redshifts, thereby testing the correlations between Mg II and Lyα (and maybe LyC) closer to the EOR.

X.X. and A.H. acknowledge support from NASA STScI grants GO 15865. A.S.-L. and D.S. acknowledge support from the Swiss National Science Foundation. M.T. acknowledges support from the NWO grant 0.16.VIDI.189.162 ("ODIN"). This research has made use of the NASA/IPAC Infrared Science Archive, which is funded by the National Aeronautics and Space Administration and operated by the California Institute of Technology.

Facilities: HST(COS), SDSS, IRSA.

Software: astropy (The Astropy Collaboration 2013, 2018), BPASS (v2.2.1, Stanway & Eldridge 2018), CalCOS (STScI), CLOUDY (v17.01; Ferland et al. 2017), FaintCOS (Makan et al. 2021), jupyter (Kluyver 2016), MPFIT (Markwardt 2009), python, Prospector (Johnson et al. 2019; Leja et al. 2017), PyNeb (Luridiana et al. 2015).

ORCID iDs

Xinfeng Xu https://orcid.org/0000-0002-9217-7051
Alaina Henry https://orcid.org/0000-0002-6586-4446
Timothy Heckman https://orcid.org/0000-0001-6670-6370
John Chisholm https://orcid.org/0000-0002-0302-2577
Gábor Worseck https://orcid.org/0000-0003-0960-3580
Max Gronke https://orcid.org/0000-0003-2491-060X
Anne Jaskot https://orcid.org/0000-0002-6790-5125
Stephan R. McCandliss https://orcid.org/0000-0003-0503-4667
Sophia R. Flury https://orcid.org/0000-0002-0159-2613
Mauro Giavalisco https://orcid.org/0000-0002-7831-8751
Zhiyuan Ji https://orcid.org/0000-0001-7673-2257
Ricardo O. Amorín https://orcid.org/0000-0001-5758-1000
Danielle A. Berg https://orcid.org/0000-0002-4153-053X
Sanchayeeta Borthakur https://orcid.org/0000-0002-2724-8298
Nicolas Bouche https://orcid.org/0000-0003-0068-9920
Cody Carr https://orcid.org/0000-0003-4166-2855
Dawn K. Erb https://orcid.org/0000-0001-9714-2758
Matthew Hayes https://orcid.org/0000-0001-8587-218X
Kirill Makan https://orcid.org/0000-0003-3157-1191
Rui Marques-Chaves https://orcid.org/0000-0001-8442-1846
Michael Rutkowski https://orcid.org/0000-0003-3527-1428
Göran Östlin https://orcid.org/0000-0002-3005-1349
Marc Rafelski https://orcid.org/0000-0002-9946-4731
Alberto Saldana-Lopez https://orcid.org/0000-0001-8419-3062
Claudia Scarlata https://orcid.org/0000-0002-9136-8876
Daniel Schaerer https://orcid.org/0000-0001-7144-7182
Maxime Trebitsch https://orcid.org/0000-0002-6849-5375
Christy Tremonti https://orcid.org/0000-0003-3097-5178
Anne Verhamme https://orcid.org/0000-0002-2201-1865
Bingjie Wang https://orcid.org/0000-0001-9269-5046

References

Akritas, M. G., & Siebert, J. 1996, MNRAS, 278, 919
Alexandroff, R. M., Heckman, T. M., Borthakur, S., Overzier, R., & Leitherer, C. 2015, ApJ, 810, 104
Andrews, B. H., & Martini, P. 2013, ApJ, 765, 140
Bañados, E., Venemans, B. P., Mazzucchelli, C., et al. 2018, Natur, 553, 473
Baldwin, J. A., Phillips, M. M., & Terlevich, R. 1981, PASP, 93, 5
Becker, G. D., D'Aloisio, A., Christenson, H. M., et al. 2021, MNRAS, 508, 1853
Becker, R. H., Fan, X., White, R. L., et al. 2001, AJ, 122, 2850
Berg, D. A., Chisholm, J., Erb, D. K., et al. 2019, ApJL, 878, L3
Bergvall, N., Zackrisson, E., Andersson, B. G., et al. 2006, A&A, 448, 513
Borthakur, S., Heckman, T. M., Leitherer, C., & Overzier, R. A. 2014, Sci, 346, 216
Bouwens, R. J., Oesch, P. A., Stefanon, M., et al. 2021, AJ, 162, 47
Calzetti, D., Armus, L., Bohlin, R. C., et al. 2000, ApJ, 533, 682
Cardelli, J. A., Clayton, G. C., & Mathis, J. S. 1989, ApJ, 345, 245
Chabrier, G. 2003, PASP, 115, 763
Chevallard, J., Charlot, S., Senchyna, P., et al. 2018, MNRAS, 479, 3264
Chisholm, J., Prochaska, J. X., Schaerer, D., Gazagnes, S., & Henry, A. 2020, MNRAS, 498, 2554
Conroy, C., Gunn, J. E., & White, M. 2009, ApJ, 699, 486
de Kool, M., Becker, R. H., Gregg, M. D., White, R. L., & Arav, N. 2002, ApJ, 567, 58
Dijkstra, M., Gronke, M., & Venkatesan, A. 2016, ApJ, 828, 71
Duncan, K., & Conselice, C. J. 2015, MNRAS, 451, 2030
Eldridge, J. J., Stanway, E. R., Xiao, L., et al. 2017, PASA, 34, e058
Fan, X., Strauss, M. A., Becker, R. H., et al. 2006, AJ, 132, 117
Feldman, G. J., & Cousins, R. D. 1998, PhRvD, 57, 3873
Ferland, G. J., Chatzikos, M., Guzmán, F., et al. 2017, RMxAA, 53, 385
Finkelstein, S. L., D'Aloisio, A., Paardekooper, J.-P., et al. 2019, ApJ, 879, 36
Flury, S. R., Jaskot, A. E., Ferguson, H. C., et al. 2022a, ApJS, 260, 1
Flury, S. R., Jaskot, A. E., Ferguson, H. C., et al. 2022b, ApJ, 930, 126
Gazagnes, S., Chisholm, J., Schaerer, D., Verhamme, A., & Izotov, Y. 2020, A&A, 639, A85
Gazagnes, S., Chisholm, J., Schaerer, D., et al. 2018, A&A, 616, A29
Giallongo, E., Grazian, A., Fiore, F., et al. 2015, A&A, 578, A83
Grazian, A., Giallongo, E., Fiore, F., et al. 2020, ApJ, 897, 94
Grevesse, N., Asplund, M., Sauval, A. J., & Scott, P. 2010, Ap&SS, 328, 179
Gronke, M., Dijkstra, M., McCourt, M., & Oh, S. P. 2016, ApJL, 833, L26
Gronke, M., Dijkstra, M., McCourt, M., & Oh, S. P. 2017, A&A, 607, A71
Gronke, M., Ocvirk, P., Mason, C., et al. 2021, MNRAS, 508, 3697
Guseva, N. G., Izotov, Y. I., Fricke, K. J., & Henkel, C. 2013, A&A, 555, A90
Guseva, N. G., Izotov, Y. I., Schaerer, D., et al. 2020, MNRAS, 497, 4293
Hayes, M., Schaerer, D., Östlin, G., et al. 2011, ApJ, 730, 8
Hayes, M. J., Runnholm, A., Gronke, M., & Scarlata, C. 2021, ApJ, 908, 36
Heckman, T. M., Borthakur, S., Overzier, R., et al. 2011, ApJ, 730, 5
Heckman, T. M., Sembach, K. R., Meurer, G. R., et al. 2001, ApJ, 558, 56
Henry, A., Berg, D. A., Scarlata, C., Verhamme, A., & Erb, D. 2018, ApJ, 855, 96
Henry, A., Rafelski, M., Sunnquist, B., et al. 2021, ApJ, 919, 143
Henry, A., Scarlata, C., Martin, C. L., & Erb, D. 2015, ApJ, 809, 19
Hopkins, P. F., Hernquist, L., Cox, T. J., & Kereš, D. 2008, ApJS, 175, 356
Inoue, A. K., Shimizu, I., Iwata, I., & Tanaka, M. 2014, MNRAS, 442, 1805
Izotov, Y. I., Orlitová, I., Schaerer, D., et al. 2016a, Natur, 529, 178
Izotov, Y. I., Schaerer, D., Thuan, T. X., et al. 2016b, MNRAS, 461, 3683
Izotov, Y. I., Schaerer, D., Worseck, G., et al. 2018a, MNRAS, 474, 4514
Izotov, Y. I., Worseck, G., Schaerer, D., et al. 2018b, MNRAS, 478, 4851
Izotov, Y. I., Worseck, G., Schaerer, D., et al. 2021, MNRAS, 503, 1734
Jaskot, A. E., Dowd, T., Oey, M. S., Scarlata, C., & McKinney, J. 2019, ApJ, 885, 96
Jaskot, A. E., & Oey, M. S. 2013, ApJ, 766, 91
Johnson, B. D., Leja, J., Conroy, C., & Speagle, J. S. 2021, ApJS, 254, 22
Kakiichi, K., & Gronke, M. 2021, ApJ, 908, 30
Kennicutt, R. C., & Evans, N. J. 2012, ARA&A, 50, 531
Kulkarni, G., Worseck, G., & Hennawi, J. F. 2019, MNRAS, 488, 1035
Leitet, E., Bergvall, N., Hayes, M., Linné, S., & Zackrisson, E. 2013, A&A, 553, A106
Leitherer, C., Hernandez, S., Lee, J. C., & Oey, M. S. 2016, ApJ, 823, 64
Leitherer, C., Schaerer, D., Goldader, J. D., et al. 1999, ApJS, 123, 3
Luridiana, V., Morisset, C., & Shaw, R. A. 2015, A&A, 573, A42
Madau, P., & Dickinson, M. 2014, ARA&A, 52, 415
Madau, P., & Haardt, F. 2015, ApJL, 813, L8
Madau, P., Haardt, F., & Rees, M. J. 1999, ApJ, 514, 648
Makan, K., Worseck, G., Davies, F. B., et al. 2021, ApJ, 912, 38
Malkan, M. A., & Malkan, B. K. 2021, ApJ, 909, 92
Mason, C. A., Treu, T., Dijkstra, M., et al. 2018, ApJ, 856, 2
Matsuoka, Y., Strauss, M. A., Kashikawa, N., et al. 2018, ApJ, 869, 150
Naidu, R. P., Matthee, J., Oesch, P. A., et al. 2022, MNRAS, 510, 4582
Naidu, R. P., Tacchella, S., Mason, C. A., et al. 2020, ApJ, 892, 109
Nakajima, K., Ellis, R. S., Robertson, B. E., Tang, M., & Stark, D. P. 2020, ApJ, 889, 161
Nakajima, K., & Ouchi, M. 2014, MNRAS, 442, 900
Neufeld, D. A. 1990, ApJ, 350, 216
Oey, M. S., Pellegrini, E. W., Winkler, P. F., et al. 2015, HiA, 16, 587
Orlitová, I., Verhamme, A., Henry, A., et al. 2018, A&A, 616, A60
Parsa, S., Dunlop, J. S., & McLure, R. J. 2018, MNRAS, 474, 2904
Planck Collaboration, Aghanim, N., Akrami, Y., et al. 2020, A&A, 641, A6
Puschnig, J., Hayes, M., Östlin, G., et al. 2017, MNRAS, 469, 3252
Rafelski, M., Neeleman, M., Fumagalli, M., Wolfe, A. M., & Prochaska, J. X. 2014, ApJL, 782, L29
Ramambason, L., Schaerer, D., Stasińska, G., et al. 2020, A&A, 644, A21

Reddy, N. A., Steidel, C. C., Pettini, M., & Bogosavljević, M. 2016a, ApJ, 828, 107
Reddy, N. A., Steidel, C. C., Pettini, M., Bogosavljević, M., & Shapley, A. E. 2016b, ApJ, 828, 108
Rivera-Thorsen, T. E., Dahle, H., Chisholm, J., et al. 2019, Sci, 366, 738
Robertson, B. E., Ellis, R. S., Furlanetto, S. R., & Dunlop, J. S. 2015, ApJL, 802, L19
Robertson, B. E., Furlanetto, S. R., Schneider, E., et al. 2013, ApJ, 768, 71
Rosdahl, J., Katz, H., Blaizot, J., et al. 2018, MNRAS, 479, 994
Saldana-Lopez, A., Schaerer, D., Chisholm, J., et al. 2022, arXiv:2201.11800
Salpeter, E. E. 1955, ApJ, 121, 161
Scarlata, C., Colbert, J., Teplitz, H. I., et al. 2009, ApJL, 704, L98
Schenker, M. A., Ellis, R. S., Konidaris, N. P., & Stark, D. P. 2014, ApJ, 795, 20
Schlafly, E. F., & Finkbeiner, D. P. 2011, ApJ, 737, 103
Shen, X., Hopkins, P. F., Faucher-Giguère, C.-A., et al. 2020, MNRAS, 495, 3252
Shivaei, I., Reddy, N., Rieke, G., et al. 2020, ApJ, 899, 117
Stanway, E. R., & Eldridge, J. J. 2018, MNRAS, 479, 75
Stark, D. P., Ellis, R. S., & Ouchi, M. 2011, ApJL, 728, L2
Steidel, C. C., Strom, A. L., Pettini, M., et al. 2016, ApJ, 826, 159
Storey, P. J., & Hummer, D. G. 1995, MNRAS, 272, 41
Tang, M., Stark, D. P., Chevallard, J., & Charlot, S. 2019, MNRAS, 489, 2572
Trebitsch, M., Blaizot, J., Rosdahl, J., Devriendt, J., & Slyz, A. 2017, MNRAS, 470, 224
Trebitsch, M., Dubois, Y., Volonteri, M., et al. 2021, A&A, 653, A154
Verhamme, A., Orlitová, I., Schaerer, D., & Hayes, M. 2015, A&A, 578, A7
Verhamme, A., Orlitová, I., Schaerer, D., et al. 2017, A&A, 597, A13
Verhamme, A., Schaerer, D., & Maselli, A. 2006, A&A, 460, 397
Wang, B., Heckman, T. M., Amorín, R., et al. 2021, ApJ, 916, 3
Wang, B., Heckman, T. M., Leitherer, C., et al. 2019, ApJ, 885, 57
Worseck, G., Prochaska, J. X., O'Meara, J. M., et al. 2014, MNRAS, 445, 1745
Zackrisson, E., Inoue, A. K., & Jensen, H. 2013, ApJ, 777, 39